From Elasticity to Creep: Orthotropic moisture-dependent Rheology of Norway Spruce

Jonas M. Maas* Falk K. Wittel †

January 21, 2026

Abstract

In the past, numerous simulations of the long-term performance of wood components undergoing moisture changes have exhibited unresolved discrepancies with reality, pointing to misconceptions about the underlying wood's physical nature. Those are due to an incomplete and inconsistent experimental picture regarding orthotropy, moisture dependence, and the interconnection of distinct rheological mechanisms. This study, conducted on a single, homogeneous Norway spruce stem, provides a comprehensive insight into the elastic, viscoelastic, plastic, and hygroresponsive behavior in the three main anatomical directions. All data are described by generally accepted models, with moisture-scaling functions provided for each parameter. The described campaigns extend well beyond the minimum required tests for orthotropic bodies. This enables a quantitative assessment of the loss of accuracy due to symmetry assumptions, such as orthotropy and compression-tension symmetry. The completeness of the data allows for identifying oversimplifications in state-of-the-art rheological models, as well as for finding opportunities to reduce future testing effort.

Keywords: elasticity; plasticity; viscoelasticity; hygroexpansion; Norway spruce

1 Introduction

Rheological models for wood have reached a high level of sophistication for describing moisture-dependent elastic, plastic (e.g., Schmidt and Kaliske, 2006; Kaliske et al., 2010; Mackenzie-Helnwein et al., 2003; Benvenuti et al., 2020), hygroexpansive, viscoelastic (e.g., Hanhijärvi and Mackenzie-Helnwein, 2003; Fortino et al., 2009), and mechanosorptive (e.g., Fortino et al., 2009; Yu et al., 2022) behavior. For their implementation, experimental parameters from numerous independent studies need to be combined (Hassani et al.,

*ETH Zurich, Institute for Building Materials, HIF E 27, Laura-Hezner-Weg 7, CH-8093 Zurich, Switzerland; E-mail: jomaas@ethz.ch; ORCID: 0000-0001-5679-7352

†ETH Zurich, Institute for Building Materials, HIF E 27, Laura-Hezner-Weg 7, CH-8093 Zurich, Switzerland; E-mail: fwittel@ethz.ch; ORCID: 0000-0001-8672-5464

2015; Yu et al., 2022). This typically requires compromises between data consistency and reliability, interpolation and extrapolation schemes, and scaling across different species for missing orientations. Data collections are valuable resources; however, they convey a false sense of completeness, as various isolated studies that often share only the species are aggregated and combined (Ross, 2021; Niemz et al., 2025). For all species, the completeness of mechanical parameters strongly depends on the rheological mechanism.

Moisture-dependent **elastic properties** are well-researched, and key literature like Kollmann and Côté (1968), Ross (2021), or Niemz et al. (2023) provides orthotropic elastic parameters for a vast collection of species. These parameters commonly relate to a specific moisture content (MC), except for Neuhaus (1981), who published the complete moisture-dependent orthotropic elastic compliance for Norway spruce (*Picea abies*). He identified the compliance matrix on uniaxial tension and torsion tests at eight different MCs. Numerous moisture-dependent studies for various species followed, e.g., for European beech (*Fagus sylvatica*) (Ożyhar et al., 2013; Hering et al., 2012a), common ash (*Fraxinus excelsior*) (Niemz et al., 2014), or Chinese fir (*Cunninghamia lanceolata*) (Jiang et al., 2017). Young's moduli and Poisson's ratios in these tests originate from uniaxial tests, whereas shear moduli were indirectly derived from ultrasonic tests. In contrast, direct mechanical tests of all six moisture-dependent shear moduli of Norway spruce were provided by Dahl and Malo (2009a) from Arcan tests, but only at 65% relative humidity (RH).

Studies on wood **plasticity** are fragmented as well, as studies focus on specific loading directions at one MC, most commonly at 20 °C and 65 %RH (e.g., Adalian and Morlier, 2002; Yoshihara, 2009; Akter and Bader, 2020; Al-musawi et al., 2024). Milch et al. (2016) determined non-linear isotropic plastic hardening under compression and tension in the longitudinal (L), radial (R), and tangential (T) directions. For shear plasticity, Dahl and Malo (2009b) quantified exponential hardening in all six shear planes (RT, TR, RL, LR, TL, LT) via Arcan tests. Note that the first index of the shear plane denotes its normal direction, while the second index gives the direction of the acting force. Biaxial stress states were studied by Eberhardsteiner (2002) and Fleischmann (2005), who provided failure envelopes for the LR and LT stress planes, as well as the biaxial stress-strain relationships. Their results provided the experimental basis for several multisurface plasticity models (e.g., Mackenzie-Helnwein et al., 2003; Schmidt and Kaliske, 2006), even though moisture dependence could not be directly addressed. Studies respecting multiple stress states and MCs for Norway spruce remain incomplete to date (Niemz et al., 2025).

Contrary, **hygroexpansion** is well-researched, as a linear relation between swelling and shrinkage can be assumed in the MC interval $[2.5\%, 25\%]$ (Neuhaus, 1981). Ross (2021) and Niemz et al. (2023) provide collections of linear hygroexpansion coefficients for various species in R, T, and L directions.

Studies on **viscoelasticity** are commonly limited to specific orientations, MCs, or loading degrees (LDs) with respect to strength. A state-of-the-art overview can be found in Maas and Wittel (2025), who quantified all components of the orthotropic viscoelastic creep compliance tensor for Norway spruce under [20|65] climate conditions, including compression, tension, and shear asymmetry. However, moisture dependence should also be considered, as viscoelastic creep commonly increases with MC (Gressel, 1983; Hering and Niemz, 2012; Niemz et al., 2023; Ferrara and Wittel, 2025). Hofer et al. (2019) investigated temperature- and moisture-dependent creep on 3-point bending tests of Norway spruce. Unfortunately, due to the non-linear nature of creep and the resulting complex stress field in bending, such experiments cannot provide quantitative material data for simulations.

Additionally, it is vital to include creep in the transverse directions (R, T), as softwood creep in L is considerably smaller than the ones in T and R direction (see Cariou, 1987; Taniguchi et al., 2010; Maas and Wittel, 2025). To date, despite its technological importance, no study has described moisture-dependent compression, tension, and shear creep in the three main anatomical directions. The situation is comparable to that of other species. Besides the MC, the LD determines the creep rate, with a non-linear behavior for LD $> 30 - 85\%$ (Gressel, 1983; Liu, 1993). For Norway spruce, Ferrara and Wittel (2025) observed linear creep up to LD $< 50\%$ under tension.

This manuscript aims to bridge knowledge gaps by providing a comprehensive dataset on the orthotropic moisture-dependent elastic, plastic, viscoelastic, and hygroexpansive behavior of Norway spruce, originating from a single stem. For this purpose, the study conducts scleronomic and rheonomic compression, tension, and shear test campaigns with a large number of samples in the three main anatomical directions, as well as hygroresponsive tests. For data reduction, the moisture dependence of each rheological mechanism is fitted to an appropriate model: elasticity to a quadratic function, plasticity to a linearly moisture-dependent Ramberg–Osgood equation, creep to a Kelvin-Voigt (KV) series extended by the time–moisture superposition principle (TMSP), and hygroexpansion to a linear function.

The manuscript is organized as follows: The methods section (Sec. 2) summarizes the analyzed material parameters and the related model equations, followed by detailed explanations of the sample preparation and experimental procedures. The results section (Sec. 3) comprises the moisture-dependent stiffness moduli, strengths, plastic strain increments, creep compliances, and swelling coefficients. When possible, comparison is made between various anatomical directions. The subsequent discussion (Sec. 4) provides phenomenological interpretations of the observed material behavior, along with comparisons to the scientific literature. All data and evaluation procedures are open access and available in a Git repository.

2 Materials and methods

The dominating deformation mechanisms in wood rheology are elasticity, plasticity, viscoelasticity, mechanosorption, and hygroexpansion. Even though these mechanisms originate from a single unified deformation mechanism and are interconnected (Amando de Barros and Wittel, 2024), strict separation of those rheological mechanisms is useful for simplicity and extensibility. Hence, sophisticated wood continuum models like Hanhijärvi and Mackenzie-Helnwein (2003), Fortino et al. (2009), Hassani et al. (2015), or Yu et al. (2022) commonly superimpose the rheological properties to a total strain $\boldsymbol{\epsilon}$:

$$\boldsymbol{\epsilon} = \boldsymbol{\epsilon}^{el} + \boldsymbol{\epsilon}^{pl} + \boldsymbol{\epsilon}^{ve} + \boldsymbol{\epsilon}^{ms} + \boldsymbol{\epsilon}^{\omega}. \tag{1}$$

The superscripts denote strains for elastic (el), plastic (pl), viscoelastic (ve), mechansorptive (ms), and hygroexpansive (ω) deformations, respectively. The strains depend on the wood's anatomical direction, loading direction, and MC.

This paper quantifies the behavior in every anatomical direction for compression, tension, and shear at various MCs, except the mechanosorptive component. Tab. A1 summarizes the experimental coverage and the corresponding determined material parameters. Fig. 1 illustrates the sample catalogue with tested orientations of the scleronomic and rheonomic tests.

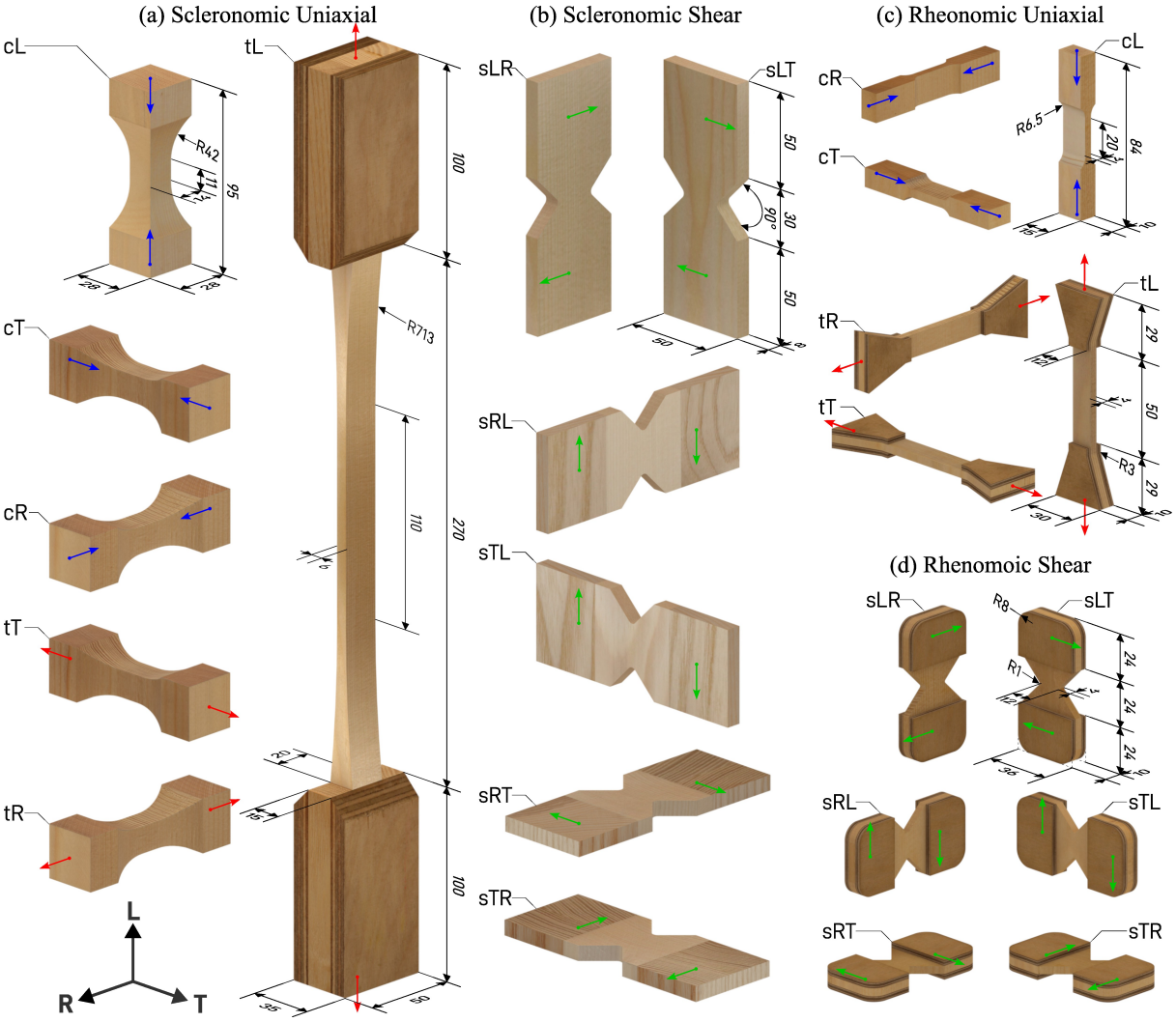

Fig. 1: Tested sample types of the (a) uniaxial scleronomic, (b) shear scleronomic, (c) uniaxial rheonomic, and (d) shear rheonomic tests. The lower case letters indicate the loading type (compression c, tension t, shear s), and the upper case letters the loading direction. Arrows indicate compression (blue), tension (red), and shear (green) forces.

2.1 Model equations

The use of models is a convenient way of data reduction by describing the behavior with a reduced set of parameters. This paper utilizes the subsequent equations to describe elasticity, plasticity, viscoelasticity, sorption, and hygroexpansion of the hygro-elastic orthotropic body. All equations use the Voigt notation and are formulated using the Einstein summation convention.

Elasticity The elastic strain $\boldsymbol{\epsilon}^{el}$ of the orthotopic body can be idealized as linearly dependent on the stress $\boldsymbol{\sigma}$ by Hooke's law (Kollmann and Côté, 1968; Niemz et al., 2023):

$$\epsilon_i^{el} = C_{0,ij}^{-1}\sigma_j \quad \text{with} \quad \boldsymbol{C}_0^{-1} = C_{0,ij}^{-1} = \begin{bmatrix} \frac{1}{E_R} & \frac{-\nu_{TR}}{E_T} & \frac{-\nu_{LR}}{E_L} & 0 & 0 & 0 \\ \frac{-\nu_{RT}}{E_R} & \frac{1}{E_T} & \frac{-\nu_{LT}}{E_L} & 0 & 0 & 0 \\ \frac{-\nu_{RL}}{E_R} & \frac{-\nu_{TL}}{E_T} & \frac{1}{E_L} & 0 & 0 & 0 \\ 0 & 0 & 0 & \frac{1}{G_{RT}} & 0 & 0 \\ 0 & 0 & 0 & 0 & \frac{1}{G_{RL}} & 0 \\ 0 & 0 & 0 & & 0 & 0 \quad \frac{1}{G_{TL}} \end{bmatrix}. \tag{2}$$

The elastic compliance matrix $\boldsymbol{C}_0^{-1}$ is defined by the Young's moduli E_i in direction $i \in \{R, T, L\}$, Poisson's ratios ν_{ji} as the negative ratio of the strain in direction i and the one in load direction j, and shear moduli G_{ij} acting in a shear plane normal to i in loading direction j. To fulfill the orthotropy conditions, the equations

$$\frac{\nu_{ij}}{E_i} = \frac{\nu_{ji}}{E_j} \quad \text{and} \quad G_{ij} = G_{ji} \tag{3}$$

must hold and $\boldsymbol{C}_0^{-1}$ must be positive definite (Kienzler and Schröder, 2019).

Plasticity Hering et al. (2012b) successfully expressed wood plasticity with the relation by Ramberg and Osgood (1943). When omitting lateral plastic strains, it can be expressed in Voigt notation by

$$\epsilon_i^{pl} = \left(\frac{\sigma_i}{K_i}\right)^{n_i} \quad \text{for} \quad \sigma_i < f_i, \tag{4}$$

with the curve-fitting parameters K_i and n_i, and the material strengths f_i. Note that the equation cannot describe strain softening, as Eq. 4 only monotonically increases with stress (Bodig and Jayne, 1982).

Viscoelasticity Maxwell or KV elements are a common modeling approach for viscoelasticity (Gutierrez-Lemini, 2014; Hajikarimi and Moghadas Nejad, 2021). KV elements are advantageous because parameters can be identified in creep tests, and strains can be easily superimposed. The time-dependent compliance component $C_{ij}^{-1}(t)$ for a series of N KV elements reads

$$C_{ij}^{-1}(t) = C_{0,ij}^{-1} + C_{\mathrm{ve},ij}^{-1}(t) = C_{0,ij}^{-1}\left(1 + \sum_{k=1}^{N} g_{k,ij}\left(1 - \mathrm{e}^{-t/\tau_{k,ij}}\right)\right). \tag{5}$$

t denotes the time, $C_{0,ij}^{-1}$ the elastic compliance, $C_{\mathrm{ve},ij}^{-1}(t)$ the viscoelastic creep compliance, $g_{k,ij}$ the characteristic compliance of the k-th KV element, and $\tau_{k,ij}$ the corresponding retardation time. The viscoelastic strain $\boldsymbol{\epsilon}^{ve}$ is therefore

$$\epsilon_i^{ve}(t) = C_{\mathrm{ve},ij}^{-1}(t)\sigma_j = \left(C_{0,ij}^{-1} \cdot \sum_{k=1}^{N} g_{k,ij}\left(1 - \mathrm{e}^{-t/\tau_{k,ij}}\right)\right)\sigma_j. \tag{6}$$

Higher MCs commonly accelerate the creep. One well-established approach for polymers for describing such acceleration is the TMSP (Maksimov et al., 1972). It was successfully

applied to wood by Zhan et al. (2019), Peng et al. (2022), and Zhang et al. (2024). The principle interprets a higher MC as a faster passage of time on a moisture-independent master creep curve $\epsilon_i^{\text{ve,master}}(t')$. A shift function $a_\omega(\omega)$ maps the true time t to conventional time t' (Maksimov et al., 1972), resulting in the moisture-dependent creep curve

$$\epsilon_i^{ve}(t,\omega) = \epsilon_i^{\text{ve,master}}(t') \quad \text{with} \quad t' = a_\omega(\omega)\cdot t. \tag{7}$$

According to Hajikarimi and Moghadas Nejad (2021), a KV series or a Maxwell series can describe the master creep curve. The shift function for polymers is typically a Williams-Landel-Ferry (WLF) type equation. However, sorption mechanisms in wood differ from those in homogeneous polymers and vary over MC. Thus, this paper utilizes the empirical logistic function

$$\ln(a_\omega(\omega)) = p_0 + \frac{\ln(a_R) - p_0}{1+\exp(p_1-\omega)} \tag{8}$$

to describe the time shifts. p_0 and p_1 are fitting parameters, and a_R is the maximum time shift across the highest tested RH. The function was chosen, as it converges to constant values in the extrapolation range. Note that in limited experimental ranges, other interpolation functions might be more appropriate (Ferrara and Wittel, 2025).

Sorption Wood's scleronomic and rheonomic properties vary with the MC

$$\omega(\varphi) = (m(\varphi) - m_0)/m_0, \tag{9}$$

where $m(\varphi)$ is the wood mass at the environment's RH φ, and m_0 is the wood's oven-dry mass. Sorption isotherms commonly describe the relationship between ω and φ, which exhibits a hysteresis between ad- and desorption. Common models for describing the moisture isotherm are the two-hydrate model by Hailwood and Horrobin (1946) (Simpson, 1973; Ross, 2021) and its one-hydrate form (Skaar, 1988), which can be expressed in the form by Dent (1977) as

$$\omega(\varphi) = \frac{\varphi}{A + B\varphi - C\varphi^2}. \tag{10}$$

A, B, and C are the fitting parameters of the model. This paper uses the one-hydrate form because it proves more robust for fitting sorption curves with a low number of data points at low and high RHs.

Hygroexpansion With changing MC, wood expands or shrinks. The resulting hygric strain changes $\Delta\epsilon^\omega$ are idealized with linear dependence on the MC (Skaar, 1988; Hassani et al., 2015):

$$\Delta\epsilon_i^\omega = \alpha_i \Delta\omega \quad \text{with} \quad \Delta\omega = \left(\min(\omega, \omega_{FS}) - \omega_0\right). \tag{11}$$

$\Delta\epsilon_i^\omega$ is the hygroexpansive strain change in direction $i \in \{R,T,L\}$ relative to the initial MC ω_0. α_i is the corresponding hygroexpansion coefficient, and ω_{FS} is the MC at fiber saturation, as no swelling is observed beyond fiber saturation.

2.2 Sample acquisition

All tested samples originate from the same Norway spruce stem to improve the comparability of the tested mechanical properties. The tree was harvested in winter 2021/2022 and grew at 47.065046°N and 8.710506°E at 1093 m altitude with eastern exposition in Alpthal, Switzerland. The utilized trunk section of 5 m length and approximately 40 cm diameter features a low variation in growth ring width a to approximate a homogeneous bulk material. a ranged from approximately 3 mm close to the juvenile wood to 1 mm close to the cambium. The green wood was divided into 1 m long sections, which were consecutively numbered and cut into wedge-shaped pieces to reduce internal stresses during natural drying. After equilibrating all sections to 65% RH at 20°C, the sections were equilibrated to their testing climates. The first section provides the rheonomic and hygroresponsive samples, and the other four sections the scleronomic samples for 65%, 35%, 85%, and 95% RH. The sample geometries were sawn, planed, and ultimately milled with a routing machine upon equilibration. The area within 10 cm diameter around the pith was considered juvenile wood and excluded from the sample preparation. Because the measured mechanical properties vary with the anatomical location, especially in the R direction (Trendelenburg, 1955; Knigge and Schulz, 1966), each sample is assigned a unique identifier `N_TYPE-XXX-YYY-ZZZ` to track its location inside the stem. `N` resembles the trunk section and `TYPE` the sample type corresponding to Fig. 1. `XXX [°]` is the polar angle relative to the trunk's primary cut, `YYY [mm]` the R coordinate from the pith, and `ZZZ [mm]` the distance from the section's bottom side to the sample's bottom side.

2.3 Scleronomic tests

The scleronomic tests comprise a substantial number of speckled samples per tested loading direction and equilibrated climate (35%, 65%, 85%, and 95% RH at 20°C, see Tab. A1). Figs. 1a and b illustrate the sample geometries, which ensure a uniform stress field in

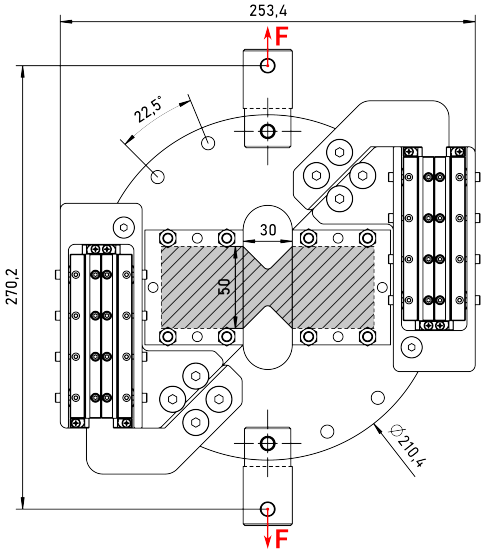

Fig. 2: Arcan sample holder. F is the applied force direction, exerting a shear force onto the sample (highlighted gray). Linear rails ensure that the sample holders cannot rotate relative to each other, permitting only relative vertical movements.

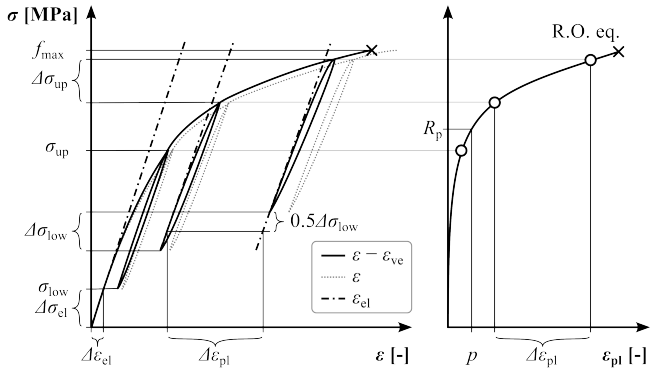

Fig. 3: Stress-strain relationships of the scleronomic tests (left). The elastic strain ϵ_{el} resembles the initial tangent modulus $E = \Delta\sigma_{el}/\Delta\epsilon_{el}$ of the measured total strain ϵ subtracted by the viscoelastic strain model ϵ_{ve}. f_{max} is the ultimate strain at failure, σ_{low} and σ_{up} are the stress limits of the first load cycle with increments $\Delta\sigma_{low}$ and $\Delta\sigma_{up}$ per cycle. The plastic strain increments (right) are fitted with a Ramberg-Osgood equation (Eq. 4), where the offset stress R_p corresponds to the plastic strain p, e.g., 1 %.

the tested cross-section. The L tensile samples follow DIN 52188 (1979) with additional stabilizing birch plywood cap strips in the clamping regions. The other tension and all compression samples follow the 3D dogbone shape used by Keunecke et al. (2008). The shear samples are Arcan samples, inspired by Müller et al. (2015) and Bachtiar et al. (2017). Unlike compression and tension, the Arcan tests are an improved version of the standard procedures, featuring a set of two additional linear rails as illustrated in Fig. 2. These rails prevent spurious relative rotation between the sample holders, which would otherwise induce a bending moment in the tested cross-section.

The samples were cyclically loaded to failure with increasing load increments using a Zwick Z100 universal testing machine, following the stress-strain relationships in Fig. 3. The load cell was a Zwick 100kN GTM with $< 0.28\%$ relative accuracy above 200N for the uniaxial tests and a Zwick 10kN KAF with $< 0.25\%$ relative accuracy above 20N for the shear tests. Two cameras recorded two perpendicular sample surfaces. Tab. A2 gives the camera resolution, recording interval T, loading rate $\dot{\sigma}$, lower and upper stress of the first load cycle σ_{low} and σ_{up}, and their respective increment per load cycle $\Delta\sigma_{low}$ and $\Delta\sigma_{up}$ for each type of experiment.

Digital Image Correlation (DIC) via Matlab Ncorr (Blaber et al., 2015) was used to estimate the Green-Lagrangian strains from the acquired images. Matlab's standard camera calibration algorithm (The MathWorks Inc., 2022) was used to correct for lens distortions. By recording images of perpendicular surfaces, each camera tracks the lateral displacement of the other camera's sample surface. Using the optical relationships in Sutton et al. (2008), the bias-error due to in-plane movements is corrected for the other camera's strain field. By averaging over a region of interest (ROI), the strain fields are reduced to scalars with a measured temporal noise-floor of $1 \cdot 10^{-5}$. If possible, the ROI was aligned with the annual rings to ensure an equal latewood-to-earlywood ratio. Otherwise, the ROI had a fixed margin at the sample edges.

At least three additional short-term creep tests per sample type captured the linear creep behavior. Those creep tests measured 1 min creep and 1 min relaxation in cyclic tests with increasing LDs. A linear creep model with two KV elements ($\boldsymbol{\tau} = [5, 60]$ s) fitted the creep curves. After correcting the elasto-plastic tests with that creep model, a

linear least-squares fit with Python SciPy (Virtanen et al., 2020) determined the linear-elastic properties of the first load cycles. From the unloading curves, the plastic strain increments were determined. The plastic properties per sample, however, derive from fitting the Ramberg-Osgood equation (Eq. 4) with Python Lmfit (Newville et al., 2025) over these plastic increments. Measuring each sample's weight with a Mettler AE 200 (0.1 mg precision) before a test and its oven-dry mass according to DIN EN 13183-1 (2002) gave the respective MCs.

2.4 Rheonomic tests

The viscoelastic experiments follow the methodology described in Maas and Wittel (2025). The experiments utilize a computer-controlled, climatized creep rack and the sample geometries outlined in Figs. 1c and d. The samples are 4 mm thick for later applicability in mechanosorptive tests with short equilibration times, while having at least four annual rings across their cross-section to represent a homogeneous bulk material. Tab. 1 summarizes the LDs of the tested creep samples. The tests comprise multiple creep test realizations for compression, tension, and shear per anatomical direction and climate (35 %, 65 %, and 90 % RH at $23 \pm 2\,^{\circ}\mathrm{C}$) for 30 days. 2D DIC with a measured temporal noise-floor of $4 \cdot 10^{-5}$ tracked strain deformations at a 3-hour measurement interval. The LD with respect to the scleronomic tests' average sample strengths was set below 40 % to ensure linear creep (Gressel, 1983; Schniewind, 1968). A least-squares optimization with SciPy (Virtanen et al., 2020) was used to fit the KV model compliances from Eq. 6 at given $\boldsymbol{\tau}_{ij} = [2, 20, 200, 2000]$ hours. The chosen number of elements was determined via a Fisher test (Hajikarimi et al., 2018). As a result, each creep curve requires at least three or four elements. To ensure inter-comparability, $\boldsymbol{\tau}_{ij}$ was chosen equal for all samples. Weight measurements of the accompanying twin samples at the end of each realization ensured correct MCs, as in the scleronomic test campaign.

Tab. 1: LD of the tested viscoelastic samples with their recorded axial and lateral anatomical directions. LD is relative to the scleronomic test's failure stress. Note that the true LD of shear samples might be lower, due to a low shear strength determined in Arcan tests.

RH [%]		**compression**			**tension**			**shear**					
Axial		L	R	T	L	R	T	R	T	L	T	L	R
Lateral		T	L	R	T	L	R	L	L	R	R	T	T
	35	0.33	0.33	0.24	0.28	0.23	0.24	0.23	0.26	0.22	0.31	0.23	0.44
LD	65	0.36	0.36	0.29	0.25	0.29	0.19	0.24	0.19	0.35	0.26	0.22	0.37
	90	0.29	0.39	0.29	0.26	0.30	0.40	0.25	0.23	0.33	0.29	0.26	0.48

2.5 Gravimetric sorption and hygroexansion tests

The moisture sorption isotherm measurements were made by determining the mass of 20 cuboid samples, successively equilibrated to the RHs $\boldsymbol{\varphi} = \{6.7, 29.7, 29.3, 59.9, 66.7, 80.4, 86.3, 93.4, 87.8, 82.4, 71.7, 57.5, 40.4, 31.1, 5.5\}\%$ at $21.4 \pm 1.6\,^{\circ}\mathrm{C}$. Thus, the tests do not comprise the green wood's first desorption path. The sample dimensions (R × T × L) at 65% RH during storage are $33.90 \pm 0.03 \times 39.57 \pm 0.03 \times 20.04 \pm 0.05$ mm, with a weight of 9.61 ± 0.44 g. All samples originated from locations 93 mm distant from the pith.

When climate chambers were unavailable, sealed boxes containing saturated salt solutions were used. Following Greenspan (1977), the salt solutions were potassium acetate for 23%, magnesium chloride for 33%, ammonium chloride for 79%, and potassium chloride for 85% target RH at 20 °C. During equilibration, a Voltcraft DL-121TH multi-datalogger monitored the climate with an accuracy of ±3% RH and ±1 °C between 0 to 100% RH. A Mettler Toledo PM200 weight scale with 0.001 g precision was used to determine the equilibrium mass after at least 14 days of equilibration. After the sorption test, the samples were dried at 103 ± 2 °C to determine their oven-dry masses, following DIN EN 13183-1 (2002). A last adsorption test was carried out after over-drying to provide an additional data point at 6.6% RH on the adsorption path.

The oven-dry density originates from an independent set of 62 cuboid samples, following DIN 52182 (1976) with oven-dry dimensions (R × T × L) of $19.67 \pm 0.07 \times 15.42 \pm 0.08 \times 94.79 \pm 0.05$ mm and an average mass of 10.81 ± 0.66 g. They were extracted at different R positions $r \in \{50, 75, 96, 119, 140, 162, 184\}$ mm from the pith. The lengths were measured with a Mitutoyo Digimatic indicator IDF-122 with 0.001 mm accuracy.

A distinct set of samples was prepared to determine the hygroexpansion coefficients, which were measured under conditions identical to those of the sorption samples. Various sample dimensions (R × T × L) were prepared for hygroexpansion measurements: in the R direction 108 × 4 × 30 mm, in T 30 × 108 × 4 mm, and in L 30 × 4 × 490 mm. The distance of the samples to the pith was 137 mm (R), 176 mm (T), and 96 ± 23 mm (L). The test campaign comprised ten samples of each direction. The maximum dimension of the samples was measured at four evenly distributed points along the sample width using the IDF-122 digimatic indicator. The strains $\epsilon_i^\omega(\omega)$ were derived by normalizing the length $l_i(\omega)$ in the direction $i \in \{R, T, L\}$ with the computed oven-dry length $l_{i,dry}$ as $\epsilon_i^\omega(\omega) = (l_i(\omega) - l_{i,dry})/l_{i,dry}$.

3 Results

All results for each rheological property are expressed by moisture-dependent functions, fitted to the respective property's statistical scatter. Given that multiple fitting approaches are possible, this study provides the entire dataset for readers to perform alternative evaluations. The scleronomic tests are the origin of the moisture-dependent elastic stiffnesses, strengths, and plastic strains in all anatomical directions. The rheonomic tests provide the complete moisture-dependent viscoelastic compliance matrix, and the hygroresponsive tests give hygroexpansion coefficients in all uniaxial directions, the sorption isotherm, and moisture-dependent densities at varying distances from the pith.

3.1 Scleronomic properties

Each scleronomic experiment provides the stress-strain relationship of an incrementally loaded sample, with the maximum load increasing in each successive loading cycle until failure. The samples' stress-strain relationships (Fig. 3) provide initial elastic stiffnesses, failure strengths, and plastic strain increments between each load cycle. The subsequent analysis groups the samples by anatomical direction, loading case, and tested climate.

3.1.1 Elasticity

The elastic orthotropic compliance tensor (Eq. 2) has nine independent components. Fig. 4 illustrates the reciprocal components of $\boldsymbol{C}_0^{-1}$, i.e., the measured elastic stiffnesses. While the markers indicate the experimental values, the solid lines show quadratic fits for describing the moisture dependence, with fitting coefficients summarized in Tab. A3. The black lines represent the fit using all values of a component.

For all Young's (Figs. 4a-c) and shear moduli (Figs. 4d-f), a parabolic stiffness decrease with increasing moisture is observed. While Young's moduli in the R direction (Fig. 4a) are practically identical for compression and tension, the ones in T (Fig. 4b) and L (Fig. 4c) are lower in compression than in tension. A plausible explanation could be a lower structural stability under compression. For example, DIC measurements reveal a small sideways bending motion of the T samples in the R direction due to the annual ring curvature. For the shear moduli (Figs. 4d-f), complementary planes appear nearly symmetric within the statistical variation.

The remaining reciprocal off-diagonal components of the elastic compliance tensor are plotted in Fig. 4g-i. Since orthotropy conditions require that $C_{ij}^{-1} = C_{ji}^{-1}$, $(\nu_{ij}/E_i)^{-1}$ and $(\nu_{ji}/E_j)^{-1}$ are combined as the lateral stiffness $K_{ij} = E_i/\nu_{ij} \cup E_j/\nu_{ji}$. K_{RT} (Fig. 4g) decreases with MC, showing no compression-tension asymmetry, similar to E_R. In contrast, the scatter for K_{RL} and K_{TL} (Figs. 4h-i) is substantial. Because stiffnesses are quite large, strains are small and prone to inaccuracies from DIC measurements. Fortunately, this low quality has only a negligible influence on the compliance matrix, as these terms

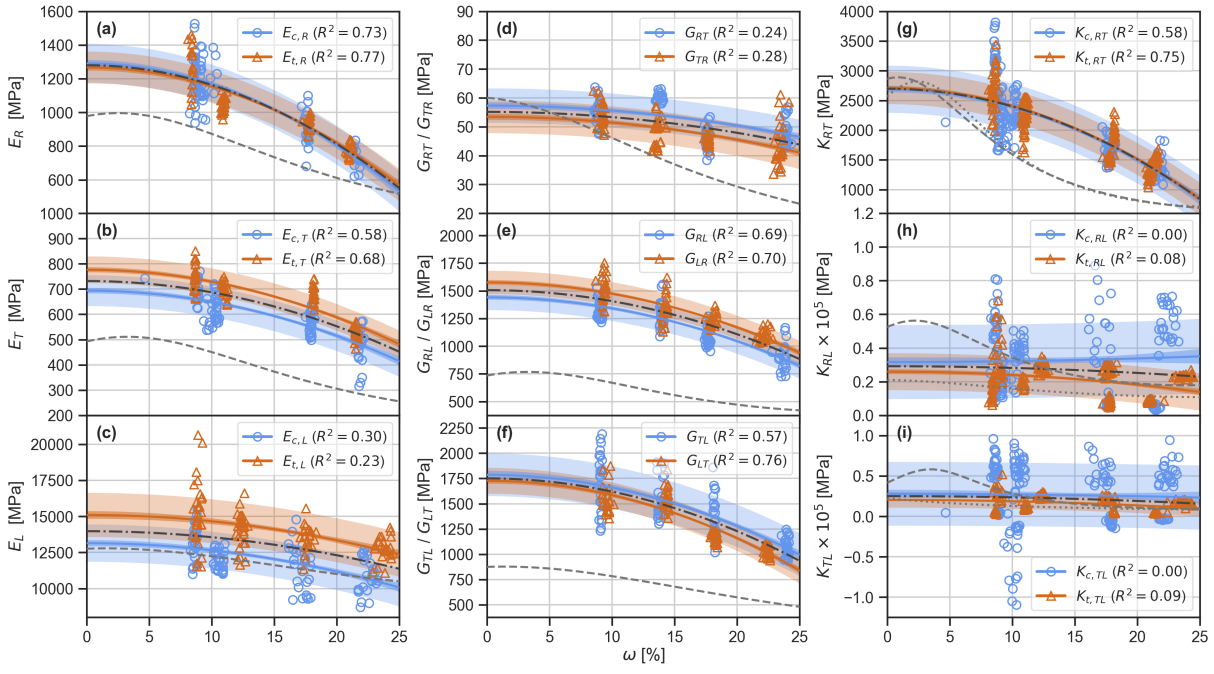

Fig. 4: Resulting Young's (a-c), shear moduli (d-f), and lateral stiffness (g-i), grouped by complementary loading directions. The solid lines depict the moisture dependence and are fitted with a 2nd order polynomial (see parameters in Tab. A3). The heavily shaded areas represent the 1-σ confidence intervals, while the lightly shaded ones give the 1-σ prediction intervals. $K_{ij} = E_i/\nu_{ij} \cup E_j/\nu_{ji}$ denotes the combined symmetric off-diagonal terms with subscript c for compression and t for tension, respectively. Black dash-dotted lines represent fits with all points of a component, while the gray dashed and dotted lines are values by Neuhaus (1981) for comparison (for K_{ij}, dashed equals E_i/ν_{ij} and dotted E_j/ν_{ji}).

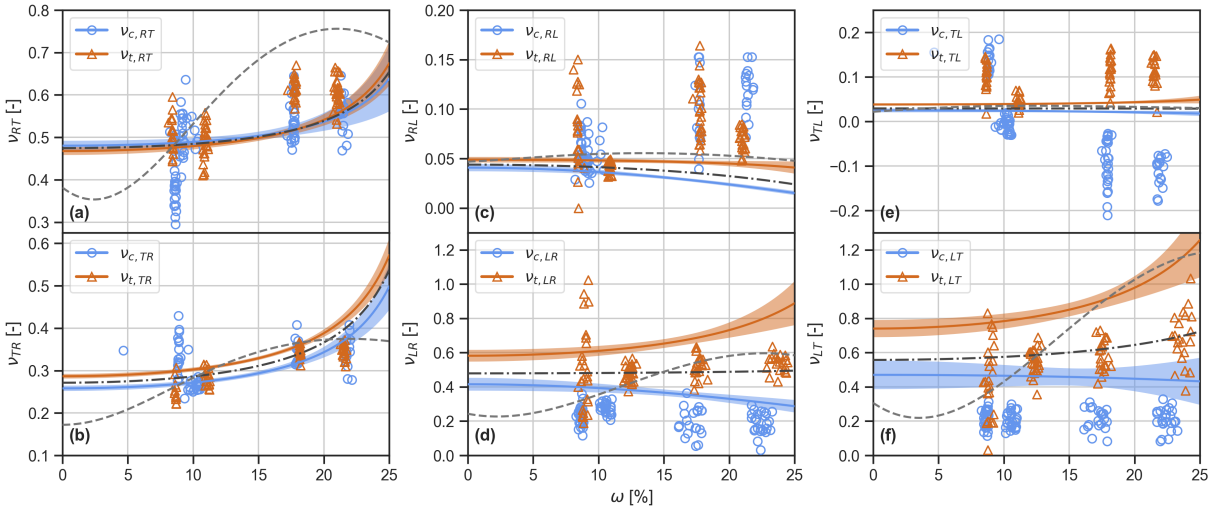

Fig. 5: Resulting Poisson's ratios ν_{ij} with loading direction i and strain direction j. Markers indicate directly measured Poisson's ratios, i.e., the negative ratio of lateral to axial strain. The solid lines are calculated from the fitted polynomials in Fig. 4 as $\nu_{ij}(\omega) = E_i(\omega)/K_{ij}(\omega)$ and therefore fulfill orthotropy with the confidence intervals propagated from Fig. 4. The black dash-dotted lines consistently represent the average between compression and tension, while the gray dashed lines depict values by Neuhaus (1981).

contribute only to a small portion of the total elastic strain. For K_{RL} and K_{TL}, only a slight decrease with moisture is observed. Note that a low R^2 indicates that no statistically sound statements can be made for the moisture-dependence of these components.

With the symmetrized compliance tensor, in principle, the required components for elasticity calculations are complete. In Finite Element (FE) packages, such as ABAQUS, one can either enter these components directly or provide engineering constants, comprising all six moduli and three Poisson's ratios. As we determine six, or even 12 ratios with tension and compression, the minimal requirements for orthotropy are overdetermined. This raises the opportunity to detect deviations from the assumed orthotropy. For this purpose, Fig. 5 compares the Poisson's ratios constructed from the fits in Fig. 4, with the non-orthotropic experimental Poisson's ratios calculated from the lateral and axial sample strains. An overlap of both indicates orthotropy of the measured Poisson's ratios, as seen for ν_{RT} and ν_{TR} (Figs. 5a-b). Deviations of markers and lines imply non-orthotropy, as evidenced for the other Poisson's ratios (Figs. 5c-f).

The experimental values of ν_{RT} (Fig. 5a) and ν_{TR} (Fig. 5b) exhibit no compression-tension asymmetry. However, the constructed lines for ν_{TR} point at a slight compression-tension asymmetry which is inherited from E_T. The data quality of the experimental ν_{RL} (Fig. 5c) and ν_{TL} (Fig. 5e) is rather low due to the very small lateral strains, resulting in a large statistical scatter and even negative values similar to Fig. 4i. In contrast, the constructed and directly measured ν_{LR} (Fig. 5d) and ν_{LT} (Fig. 5f) are consistent within the test cases. As such, the absolute lateral strains are always larger in tension than in compression for L tests. The origin of such asymmetries can be found in the kinematic behavior of the tissue. For a negative lateral strain, i.e., tension, buckling patterns as shown in Ferrara et al. (2025) might develop, which cannot emerge for positive lateral strains.

3.1.2 Strength

Strength is one of the most difficult mechanical properties to assess, as multiple moisture-dependent failure mechanisms in the cellular structure of wood interact. At the same time, it is a fundamental input property for rheological models used to predict plasticity and for creep testing. Unfortunately, the situation of literature values is incomplete with respect to anatomical directions, moisture dependence, and inter-sample material homogeneity. Additional complications arise from multiple test setups with respective sample geometries for different stress components and testing protocols, as well as microstructural features of the tree, such as density or growth ring width. In this work, the focus is set on the completeness and moisture dependence of the strength envelope, using geometries and failure criteria that assure failure under uniform stress states for the different failure stresses:

- **Tensile strength** $f_{t,i}$ in all cases $i \in \{L, R, T\}$ corresponds to the maximum stress before failure, independent of the observed failure mechanisms. Note that the scatter of values decreases for increasing MC, as wood becomes less brittle.

- **Compressive strength** is less straightforward, as stress values can continuously increase in the densification regime. In the *R direction*, samples exhibit pronounced yielding without a distinct stress peak, and the depicted strength $f_{c,R}$ is defined as the offset stress at a chosen 1% plastic strain p (see DIN 52192, 1979). Note that at $p = 1\%$, the first cell rows have already collapsed, as evidenced by strain localization seen in the DIC result. In the *T direction*, $f_{c,T}$ corresponds to the maximum stress before samples buckle due to growth ring curvature. Here, the LW layers buckle in parallel to the same direction, forming plastic hinges. Strength in *L direction* $f_{c,L}$ is defined analogously to $f_{c,T}$, however, the observed buckling pattern is characterized by kink band formation.

- **Shear strength** is always calculated from the maximum stress in Arcan tests before failure. For interpreting the different directions, however, it is essential to consider failure patterns (see Figs. 6d.1-f.2), as cracks can grow outside the region of maximal, uniform shear stress.

The obtained relationships between the strength and MC are condensed in Fig. 6 with the corresponding fitting parameters in Tab. A4. A linear model is used to describe moisture dependence, following Kollmann and Côté (1968) and Gerhards (1982).

The linear fits for strength decrease with MC coincide with the measurements. In the *R direction* (Fig. 6a), the tensile strength exceeds the compressive one from the 1% offset strain criterion. Clearly, EW tracheids debond at the growth ring interface at higher stress than their compressive counterpart, which triggers their collapse due to cell wall buckling (Huang et al., 2020; Wang et al., 2025). In contrast, in the *T direction* (Fig. 6b), the compressive strength is larger than the respective tensile one. As growth rings are parallel to the loading direction, the load is more or less taken by the LW tissue. The low tensile strength can be explained by straight preferred tracheid debonding paths, related to the cell growth direction. Under compression, LW tracheids have to collapse, which results in higher compressive strength, as the buckling length of thick LW tracheid walls is larger. In the *L direction* (Fig. 6c), the tensile strength $f_{t,L}$ is much higher than the

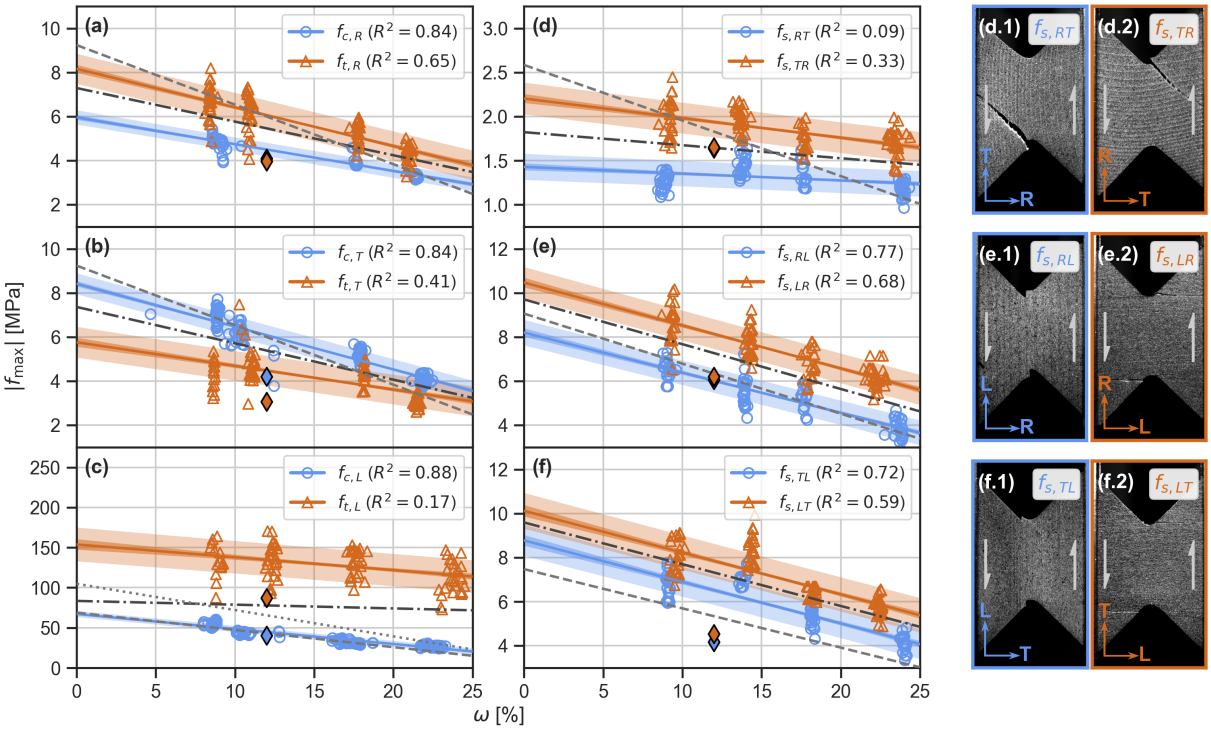

Fig. 6: Sample strength $f_{\max}$ vs. MC ω for the uniaxial loading directions (a) R, (b) T, (c) L, and shear stress in planes (d) RT / TR, (e) RL / LR, (f) TL / LT. The solid lines depict a fitted linear moisture-dependence (see parameters in Tab. A4). The heavily and weakly shaded areas represent the 1-σ confidence and prediction intervals, respectively. Typical shear fracture patterns are shown in (d.1) to (f.2) with gray arrows indicating the load case. Diamond markers depict comparative values from Niemz et al. (2023, p. 468) (a-c) and Dahl and Malo (2009b) (d-f); gray lines refer to Hassani et al. (2015) (dashed relates to blue and dotted to red cases).

compressive $f_{c,L}$. This can be explained by load alignment of tracheids, whereas under compression, fibers fail in buckling bands (Kollmann and Côté, 1968; Niemz et al., 2023).

When comparing moisture-dependent shear strengths from complementary shear planes, all configurations exhibit asymmetries. For rolling shear (Fig. 6d), the observed asymmetry is surprisingly large, with $f_{s,RT} < f_{s,TR}$. In particular, the dry RT shear samples behave in a rather brittle manner. A similar behavior was observed on tissues in Ferrara and Wittel (2024), however, their micromechanical explanation does not apply to macroscopic samples and remains unclear. For the other shear orientations (Fig. 6e-f), strength values for shear acting parallel to the fiber are lower than in cases where shear acts perpendicular to grain. Typical failure patterns for the Arcan samples are shown in (Fig. 6d.1-f.2), which are characteristic for that testing method (Dumail et al., 2000; Osei-Antwi et al., 2013; Stojcevski et al., 2018).

3.1.3 Plasticity

Before reaching its ultimate stress, wood usually exhibits plastic yielding. This fundamental mechanism redistributes forces, reduces stress concentrations, and, as such, is an essential part of wood's rheological behavior. Common modeling approaches, such as multi-surface plasticity models (e.g., Mackenzie-Helnwein et al., 2003; Schmidt and Kaliske, 2006), require yielding curves that comprise plastic hardening. They vary significantly between

anatomical directions and load cases, due to different cellular deformation mechanisms. Therefore, a key goal of the scleronomic tests is to provide moisture-dependent plastic hardening curves for compression, tension, and shear in all anatomical directions.

Every load cycle increment $\Delta\sigma_{\mathrm{up}}$ of a scleronomic test results in a plastic strain increment $\Delta\epsilon_{\mathrm{pl}}$ and a corresponding exerted stress σ (see Fig. 3). A fitted Ramberg-Osgood equation (Eq. 4) expresses this stress-plastic strain relationship for each sample. Thus, for any given offset plastic strain $p = \epsilon_{\mathrm{pl}}\,[\%]$, one can obtain the sample's respective yield stress R_{p}. Fig. 7 exemplifies this for $p = 0.02\%$ and $p = 0.2\%$, revealing an approximately linear relationship between yield stress and MC for most loading cases. The entire yield curves for varied p are shown in Fig. 8 for four different MCs, for absolute yield stresses and normalized yield stresses with respect to sample strength. The error bars correspond to the 1-σ prediction interval from Fig. 7's linear fits. In the diagrams, the ultimate strain ϵ_{ult} denotes the loading case's failure strain at the ultimate stress, averaged over all MCs. For most loading cases, the normalized stresses at ϵ_{ult} are similar, emphasizing that the ultimate plastic strain is nearly moisture-independent. Tab. A5 summarizes the parameters of the fitted moisture-dependent Ramberg-Osgood equations through Fig. 8's data points. The analysis excludes lateral plasticity as the measured strains are beyond the measurement accuracy of the tests.

As one can observe for the absolute stress-strain curves in Fig. 8, plastic strains are most pronounced for rolling shear (Figs. 8d.1 and 8d.2), as well as R and T compression (Figs. 8a.1 and 8b.1). Additionally, all loading directions, but rolling shear, experience asymmetries. Notably, R tension (Fig. 8a.2) and T tension (Fig. 8b.2) samples have much

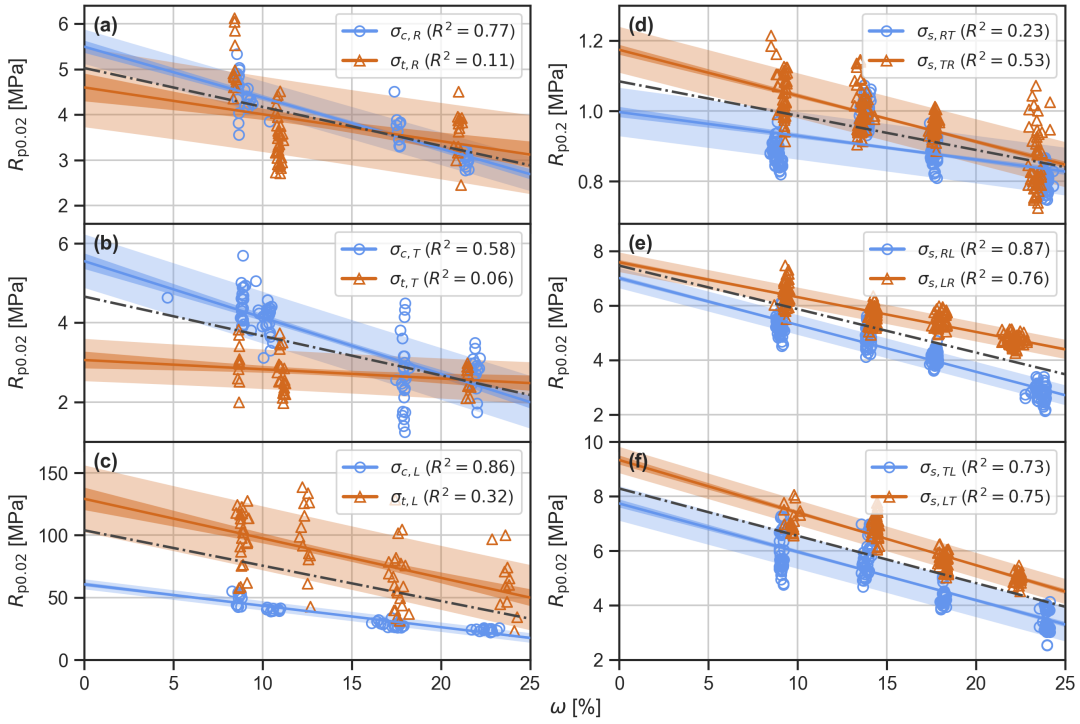

Fig. 7: Yield stress R_{p} at offset plastic strain $p\,[\%]$ for the uniaxial loading directions (a) R, (b) T, (c) L, and shear directions (d) RT / TR, (e) RL / LR, (f) TL / LT. For the shear plane ij, i is the plane's normal direction, and j is the loading direction. The heavily and weakly shaded areas represent the 1-σ confidence and prediction intervals, respectively. Note that samples where $R_{\mathrm{p}} > f_{\mathrm{max}}$ are excluded.

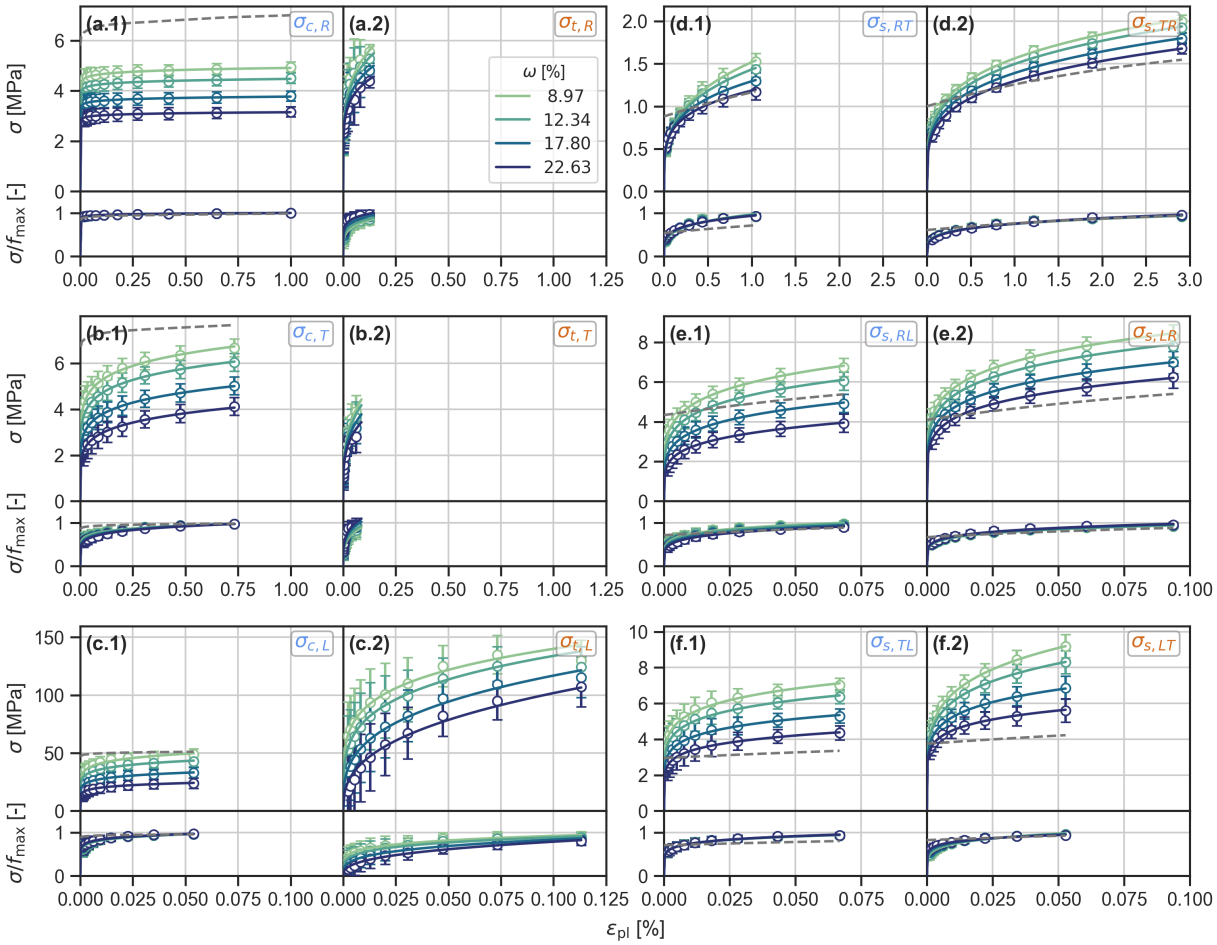

Fig. 8: Average plasticity curves for the uniaxial loading directions (a) R, (b) T, (c) L, and shear directions (d) RT / TR, (e) RL / LR, (f) TL / LT with plastic strain ϵ_{pl}, absolute stresses σ and stress normalized by strength $\sigma/f_{\max}$. $\sigma_{x,i}$ denotes the loading type x (compression c, tension t, shear s) and loading direction i. The solid lines resemble a Ramberg-Osgood equation with moisture-dependent fitting parameters (see normalized parameters in Tab. A5), and the error bars are the 1-σ prediction intervals from Fig. 7. Gray dashed lines depict comparative values at 65 % RH from Milch et al. (2016) for compression and Dahl and Malo (2009b) for shear.

lower plastic deformations than their compression counterparts, as they fail in a brittle fashion without densification. In contrast, L tension (Fig. 8c.2) exhibits larger ultimate plastic strains than L compression (Fig. 8c.1). This is a direct result of the higher strength. However, the L plastic strains at low stress levels are larger for compression than for tension. The plastic curves for shear in the RT (Fig. 8d.1) and TR (Fig. 8d.2) planes are of similar shape. One observes, that the RT shear samples fail at much lower stress (see Fig 6d), resulting in a significantly lower ultimate plastic strain. Unlike RT / TR rolling shear, the plasticity curves in the RL / LR (Figs. 8e.1 and 8e.2) and TL / LT (Figs. 8f.1 and 8f.2) shear planes exhibit low plastic deformations and show a slight asymmetry. Here, plastic strains at low stress levels are more pronounced for shear forces parallel to the fiber direction, what can be explained by the serial activation of LW and EW.

The yield curves in Fig. 8, that are normalized by the moisture-dependent strengths, result in a collapse for most anatomical directions, demonstrating that scaling by moisture-dependent strength is a valid approach, typically used in plasticity models of wood (e.g.,

Schmidt and Kaliske, 2006; Hassani et al., 2015; Yu et al., 2022). Slight discrepancies are observable in the tensile samples, though, which can be attributed to their larger statistical uncertainties.

3.2 Rhenomic properties

In timber construction, time-dependent deformations can easily exceed elastic deformations. A detailed understanding of the moisture- and direction-dependent viscoelastic behavior is therefore crucial for design. An overview of the components of the experimentally determined time- and moisture-dependent viscoelastic creep compliance tensor $C^{-1}_{\mathrm{ve},ij}(t) = C^{-1}_{ij}(t) - C^{-1}_{0,ij}$ is given in Fig. 9. To allow for better comparability with the elastic deformation and across components, all values are normalized by their respective initial elastic compliances. The tests were limited to three climatic conditions, namely 35% RH (8.0 ± 0.1% MC), 65% RH (12.5 ± 0.6% MC), and 90% RH (19.5 ± 0.3% MC) at 20 °C. The dotted lines in Fig. 9 represent the experimental datapoints, while solid lines show the best fit with the four-element KV model for each sample. The graphs indicate the following relations for the viscoelastic creep compliances:

- The R and T axial creep $\frac{1}{E_{x,R}}$ and $\frac{1}{E_{x,T}}$ (Fig. 9a) and the T lateral creep $-\frac{\nu_{x,TR}}{E_{x,T}}$ (Fig. 9c) are of comparable magnitude. Except for 8.0% MC, compression and tension creep are symmetric. The normalized creep for these components at 8.0%

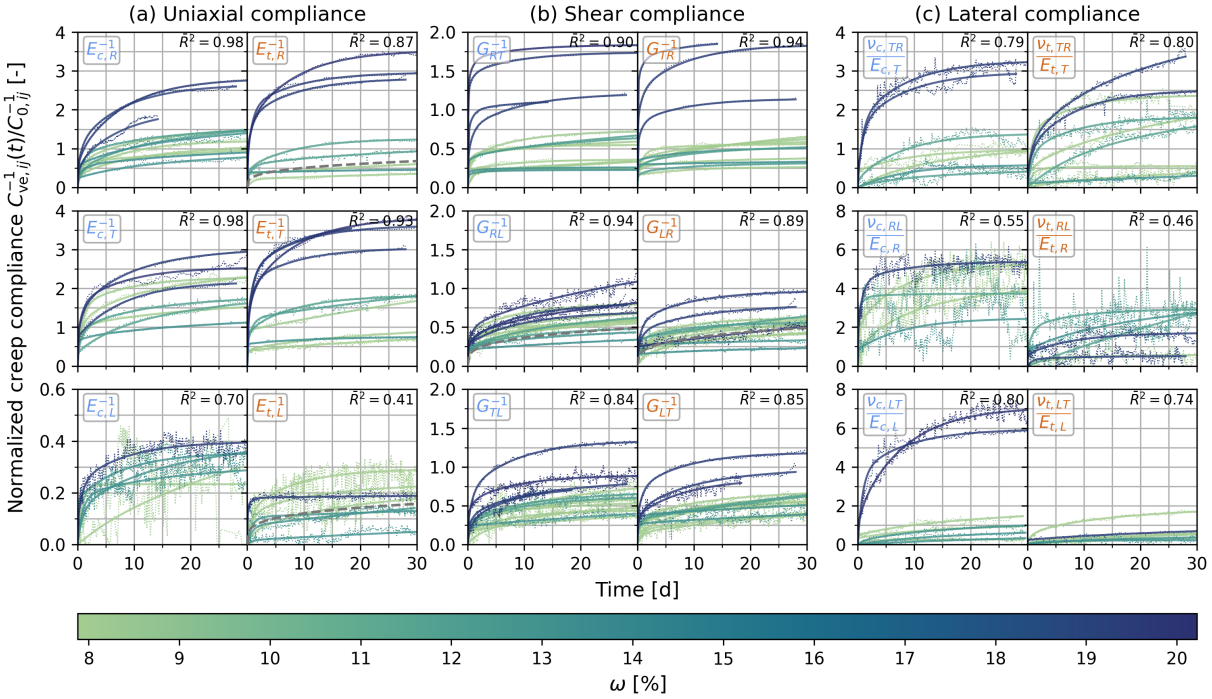

Fig. 9: Components of the creep compliance $C^{-1}_{\mathrm{ve},ij}(t)$ normalized by the initial elastic compliance $C^{-1}_{0,ij}$. The dotted and solid lines represent the experimental data and KV model fits, respectively (see Eq. 5). Components are sorted by uniaxial $1/E_{x,i}$ (a), shear $1/G_{ij}$ (b), and lateral $-\nu_{ji}/E_i$ (c) compliances with identical notation as Fig. 4. The color denotes the MC $\omega \in [8.00 \pm 0.08, 12.51 \pm 0.64, 19.59 \pm 0.33]$ %. $\bar{R}^2$ is the mean coefficient of determination per loading case. Gray dashed lines depict comparative values at 65 % RH from Hayashi et al. (1993).

and 12.5% MC is of similar magnitude, whereas at 19.6% MC it is more than twice as large.

- L axial creep $\frac{1}{E_{x,L}}$ (Fig. 9a) and its lateral component $-\frac{\nu_{x,LT}}{E_{x,L}}$ (Fig. 9c) are one magnitude smaller than creep in R and T. Consitent to observations by Gressel (1983), L creep is larger for compression than for tension. Note that, due to the small absolute creep strains and even smaller lateral ones, the measurement error is significant, leading to uncertainty in statements about its moisture dependence.

- A quite comparable moisture-dependent behavior of all shear creep components (Fig. 9b) with respect to creep in R and T is observed, only at a reduced magnitude. Furthermore, all complementary shear planes prove to be symmetric at all MCs.

- For completeness, the lateral creep for R samples $-\frac{\nu_{x,RL}}{E_{x,R}}$ (Fig. 9c) is given, even though values are below the creep rack's measurement accuracy. This is to be expected, as the Poisson's ratios ν_{RL} (Fig. 5c) vary from 0.02 to 0.05, resulting in tiny absolute strains.

In this work, KV series are used to model viscoelastic behavior. Therefore, the resulting parameter space comprises the characteristic times $\tau_{k,ij}$, the nine independent components of the compliance tensor, and the loading case asymmetries. To gain a deeper understanding of the statistical distribution of the creep curves of Fig. 9, and to obtain insight into the evolution of creep, the components of the four-parameter KV series are compared across the three discrete moisture states via boxplots in Fig. 10. One can observe

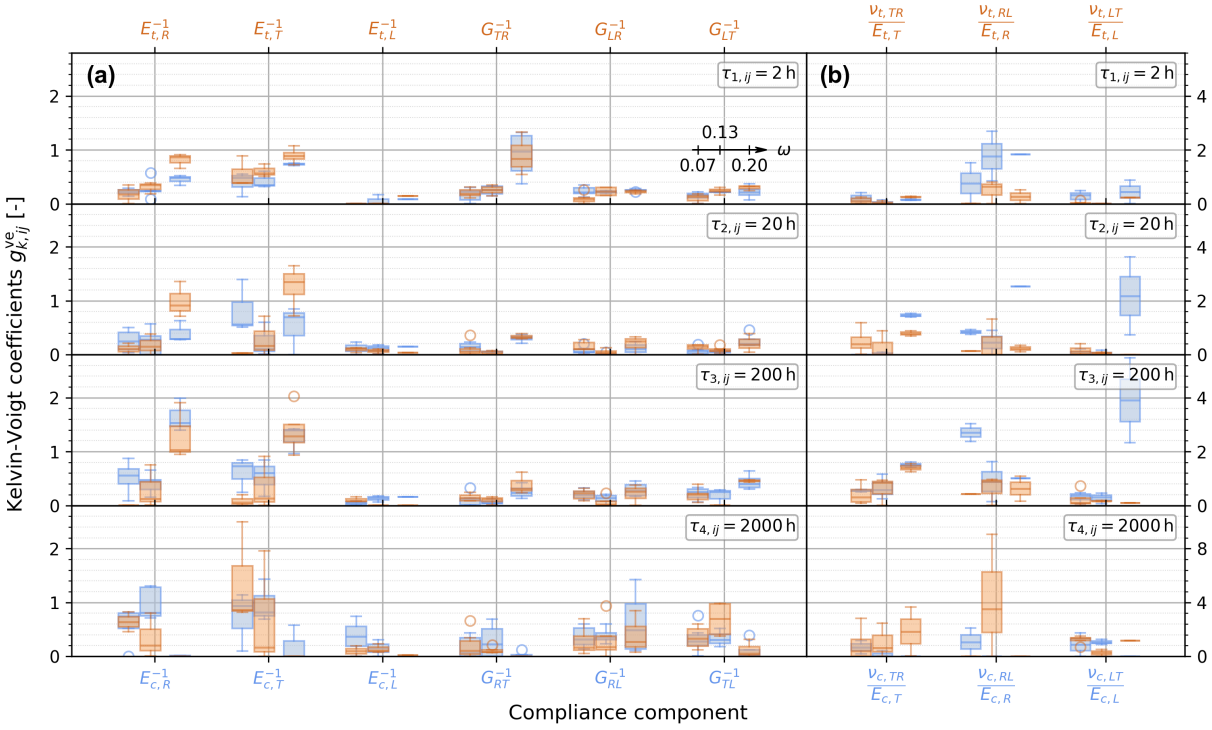

Fig. 10: KV coefficients $g^{\mathrm{ve}}_{k,ij}$ (see Eq. 5), with element index k and characteristic time $\tau_{k,ij}$. (a) represents the coefficients matching the compliance matrix's diagonal and (b) off-diagonal terms. Overlapping bars represent complementary asymmetric compliance components, similar to Fig. 9.

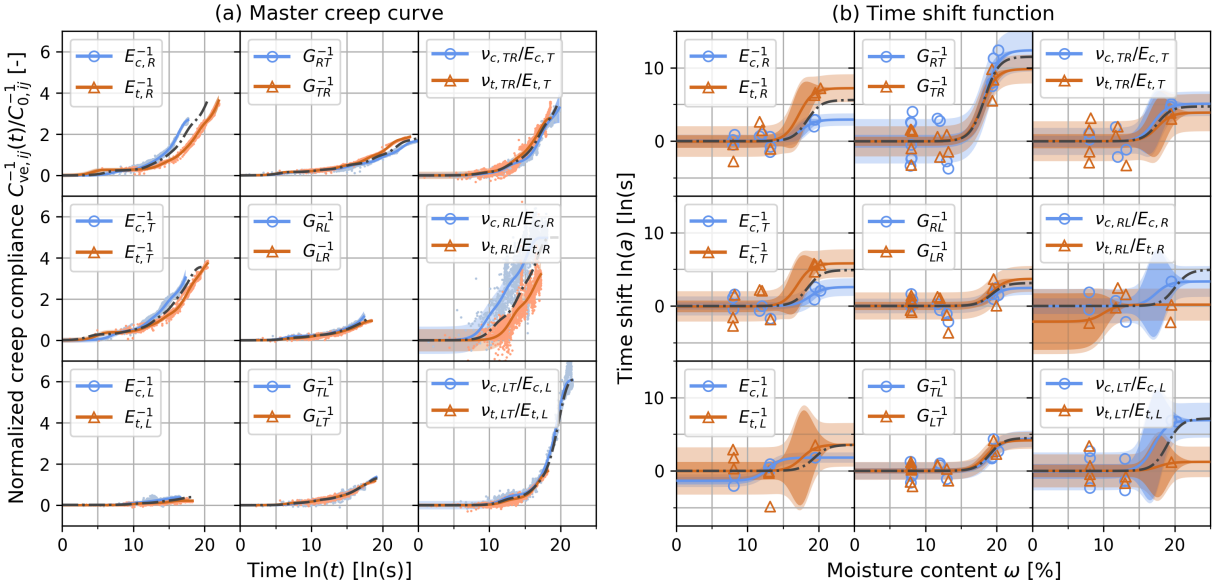

Fig. 11: TMSP fit according to Eq. 7 and parameters in Tabs. A6 and A7. (a) shows the master creep curves with a reference MC of 12.5 % and (b) gives the time shift functions for all independent creep compliance components. The black lines indicate the master creep curve and time shift function of the respective symmetrized compliance components. The heavily and weakly shaded areas represent the 1-σ confidence and prediction intervals, respectively.

a low moisture dependence for L creep (Fig. 10a) and relatively symmetric behavior for complementary shear planes. The uniaxial components show asymmetries but without a systematic pattern. This could relate to measurement inaccuracies that propagate into the parameter determination. Interestingly, most axial creep coefficients and shear creep coefficients (Fig. 10a) show an increase with moisture for the lower characteristic times $\tau_{1,ij}$ to $\tau_{3,ij}$ and a decrease for $\tau_{4,ij}$. This points to a limited creep potential that the material reaches more quickly for higher MCs.

If it is possible to consider all realizations across different moisture states for each component within a single, consistent fitting approach, statistical certainty can be considerably increased. This can be achieved via the time-moisture superposition principle (TMSP), described by Eq. 7. The master creep curves are constructed on the viscoelastic creep compliance changes $C^{-1}_{\mathrm{ve},ij}(t)$ (Maksimov et al., 1972), normalized by $C^{-1}_{0,ij}$ to eliminate the climate-dependence of the initial compliance (Kê, 1947; McCrum and Pogany, 1970). These curves result from fitting KV series models with an optimal number of elements, determined by a Fisher test (see Hajikarimi et al., 2018). Fig. 11a shows the resulting master creep curves, while Fig. 11b illustrates the corresponding time shifts as a function of the MC (see Eq. 8). The corresponding fitting coefficients are tabularized in Tabs. A6 and A7, allowing for reconstructing creep curves at arbitrary MC using Eq. 7.

The experimental results in Fig. 9 indicate that asymmetries between complementary loading cases can be omitted. As a result, data reduction can be accomplished by averaging the creep curves from complementary loading cases for each RH. To further reduce the experimental dataset required to characterize complete creep orthotropy, a k-means clustering algorithm (Virtanen et al., 2020) is applied to group these symmetrized components. The components are clustered by their normalized creep compliances measured after 30 days at 35 %, 65 %, and 90 % RH. Tab. 2 presents the resulting groups for various cluster

Tab. 2: Grouped components for different cluster counts n. d_{mean} and $d_{\max}$ denote the mean and maximum differences in $C^{-1}_{\text{ve},ij}(30\,\text{d})/C^{-1}_{0,ij}$ that occur across all tested RH between components within the same group.

n	cluster	components	d_{mean} [%]	$d_{\max}$ [%]
1	1	E_R^{-1}, E_T^{-1}, E_L^{-1}, G_{RT}^{-1}, G_{RL}^{-1}, G_{TL}^{-1}, ν_{RT}/E_T	75.6	165.5
2	1	E_R^{-1}, E_T^{-1}, ν_{RT}/E_T	22.1	50.0
	2	E_L^{-1}, G_{RT}^{-1}, G_{RL}^{-1}, G_{TL}^{-1}	54.7	136.1
3	1	E_R^{-1}, E_T^{-1}, ν_{RT}/E_T	22.1	50.0
	2	E_L^{-1}	0.0	0.0
	3	G_{RT}^{-1}, G_{RL}^{-1}, G_{TL}^{-1}	23.6	62.7
4	1	E_R^{-1}, E_T^{-1}, ν_{RT}/E_T	22.1	50.0
	2	E_L^{-1}	0.0	0.0
	3	G_{RT}^{-1}	0.0	0.0
	4	G_{RL}^{-1}, G_{TL}^{-1}	15.3	18.1
5	1	E_R^{-1}, ν_{RT}/E_T	13.0	22.3
	2	E_T^{-1}	0.0	0.0
	3	E_L^{-1}	0.0	0.0
	4	G_{RT}^{-1}	0.0	0.0
	5	G_{RL}^{-1}, G_{TL}^{-1}	15.3	18.1

counts. In this analysis, d_{mean} and $d_{\max}$ denote the mean and maximum differences in creep compliance between components within the same group, representing the maximum error introduced when the creep curve of one component is generalized to all components in that group. Increasing the number of clusters improves accuracy but requires additional experiments. For example, achieving a mean error of at most 23.6 % across all groups requires at least three clusters. The lateral components ν_{RL}/E_R and ν_{LT}/E_L are excluded due to insufficient accuracy.

3.3 Hygroresponsive properties

As all described properties strongly depend on the MC, its correct value with respect to the environmental RH is of great importance. Fig. 12 illustrates the results from the gravimetric sorption and hygroexpansion tests. The sorption isotherms in Fig. 12a have the characteristic shape of wood sorption behavior, i.e., monomolecular absorption, multimolecular absorption, and capillary condensation stages. The hysteresis between adsorption and desorption is apparent. A one-hydrate Hailwood-Horrobin model from Eq. 10 fits the sorption curve's data points with a MC at fiber saturation of $\omega_{FS} = 0.28$.

The results for hygroexpansion are shown in Fig 12b, normalized to the fit's dry length in R, T, and L direction. No hysteresis was observed between adsorption and desorption. For $i = R, T$, the relationship between ω and ϵ_i^ω is linear, and the standard deviations of the data points are marginal. The standard deviation is more prominent for $i = L$, where the swelling and shrinkage are considerably smaller. It is evident that the strain-moisture relationship is non-linear and that a piecewise linear fit is more appropriate. The obtained hygroexpansion coefficients $\boldsymbol{\alpha}^\omega = \{\alpha_R, \alpha_T, \alpha_L\} = \{0.182, 0.343, 0.017(\omega \leq 0.09) \mid 0.001(\omega > 0.09)\}$ are of similar magnitude to the values utilized by Hassani et al. (2015), which are

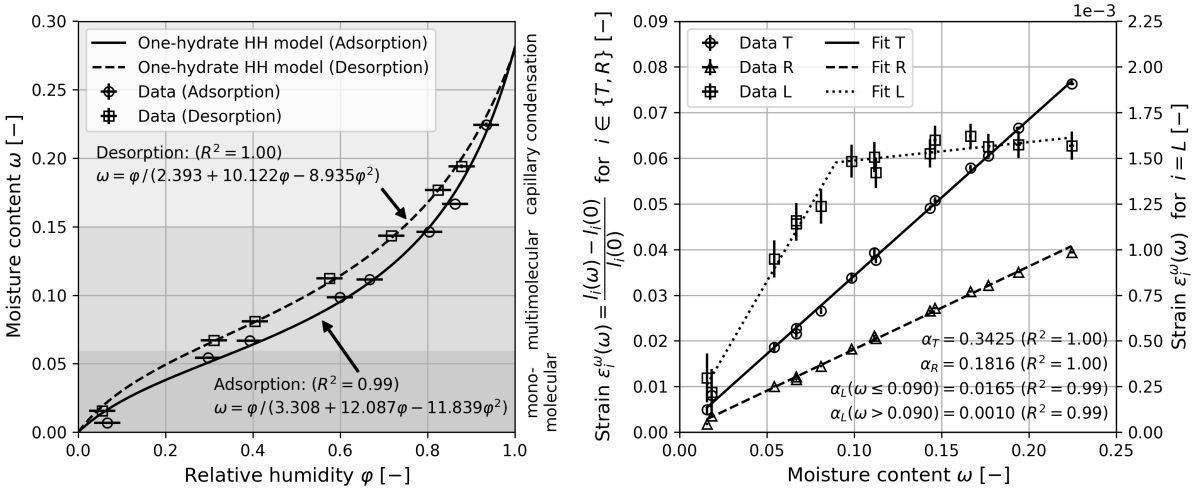

Fig. 12: Obtained sorption isotherm (a) with approximate sorption phases given in Niemz and Sonderegger (2017, p. 86), fitted with the one-hydrate Hailwood-Horrobin (HH) model (Eq. 10), and moisture-dependent hygroexpansive strains (b) (Eq. 11). α_i are the fitted linear hygroexpansion coefficients in direction $i \in \{R, T, L\}$.

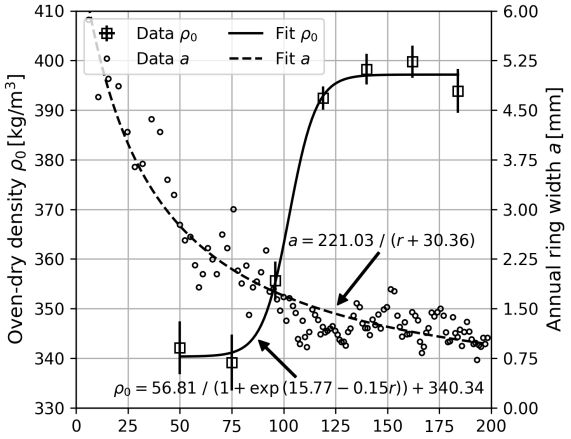

Fig. 13: Oven-dry density ρ_0 according to DIN 52182 (1976) and annual ring width a along the R coordinate r. Each density data point encompasses 8 to 10 samples. The annual ring widths were measured along a single straight line in the R direction.

$\boldsymbol{\alpha}^\omega = \{0.170, 0.330, 0.005\}$.

The sorption sample's density linearly increases with ω and can be described as $\rho(\omega) = \rho_0(1.0 + 0.4952\omega)$ with the oven-dry density in Fig. 13. According to Kollmann and Côté (1968), the density profile and oven-dry density of 390 to 400 kg/m^3 close to the cambium are characteristic of an alpine spruce.

4 Discussion

In this study, a consistent assessment of elastic, plastic, viscoelastic, and hygroexpansive orthotropy was conducted using moisture-dependent experiments. The top priority of these experiments was to achieve the highest possible data quality and cleanly isolate the respective rheological components. Hence, the employed test protocols and samples

deviate intentionally from standard codes (e.g., DIN or ASTM), which often focus on simple geometries and setups. Thus, the sample shapes are improved to achieve clean, homogeneous stress states. A second improvement is the removal of short-term linear creep from scleronomic tests, a procedure that is not commonly applied in studies of plasticity (e.g., DIN 52192, 1979; Dahl and Malo, 2009b; Hering et al., 2012b; Milch et al., 2016). Such creep can have a large influence on the soft anatomical directions at high load and moisture levels. To further reduce the influence of creep (Gressel, 1983) and cleanly assess plastic hardening, the plastic strain increments are obtained from cyclic tests with 10 to 30 load cycles. The fine and even annual rings of the samples allow for thin cross-sections compared to other studies (e.g., Gressel, 1984; Hofer et al., 2019; Akter et al., 2022; Bengtsson et al., 2024). This makes them suitable for mechanosorptive tests, as they equilibrate quickly while still representing a homogeneous bulk material. To achieve a high parameter comparability between all tests, all samples originate from a single tree, which was slowly dried and pre-cut in the green state to avoid large internal stresses during drying. The subsequent discussion compares the results to other publications, derives simplifications regarding moisture-dependent wood orthotropy, and reflects on the transferability of this work to other research studies.

4.1 Comparisons and generalizations

Comparable literature values for most rheological components are commonly restricted to specific anatomical directions and climates. For these, qualitative agreement is more significant than quantitative agreement, as experimental results inherently vary across publications due to biological variability and differences in testing protocols. In general, the comparative literature shows good qualitative agreement with this study for elasticity (Neuhaus, 1981), strength (Dahl and Malo, 2009b; Hassani et al., 2015; Niemz et al., 2023), normalized plasticity (Milch et al., 2016; Dahl and Malo, 2009b), and viscoelasticity (Hayashi et al., 1993). Furthermore, the determined sorption isotherms (Hansen, 1986), density distribution (Kollmann and Côté, 1968), and hygroexpansion (Neuhaus, 1981) are typical for alpine Norway spruce. Quantitatively, pronounced differences are mostly visible for elastic stiffness (Neuhaus, 1981) and L tensile strength (Hassani et al., 2015; Niemz et al., 2023), which are significantly lower in the literature. This difference is attributable to the fine annual ring structure of the tested tree. Based on the parameter ratios between the determined components, the following generalizations can be summarized:

- **Elasticity:** The present study provides more parameters than needed for orthotopic bodies. This way, one can assess the error associated with the orthotropy assumption. In contrast to Neuhaus (1981), also compression-tension and shear asymmetries are included. The results demonstrate, in accordance with Obara (2018) and Kumpenza et al. (2018), that spruce is not truly orthotropic. However, the non-orthotropy is small, as the difference between complementary shear planes does not exceed 16%. For ν_{RT} and ν_{TR}, the difference between symmetrized and non-symmetrized Poisson's ratios is less than 21% within the experimentally investigated moisture range. For the other Poisson's ratios, the strains are too small for reliable comparison. The largest compression-tension asymmetry is observed in the L direction with a value below 20%, which seems omitable. The moisture dependence can be best described by a quadratic function. The third-order polynomial used by Neuhaus (1981), who

tested over a wider moisture range, would lead to overfitting and an ill-conditioned covariance matrix.

- **Strength:** This study confirms a linear moisture dependence of the strength parameters, as assumed by, e.g., Gerhards (1982); Saft and Kaliske (2011) or Hassani et al. (2015). The strength varies considerably in all anatomical directions, including complementary shear planes and compression in the R and T directions.

- **Plasticity:** Many models scale yield stresses and plasticity by the respective material strength (Schmidt and Kaliske, 2006; Hassani et al., 2015; Yu et al., 2022). The present results confirm this approach, as normalization of the hardening curves by their respective moisture-dependent strengths yields a single, uniform plasticity curve. The data confirms, in agreement with Niemz et al. (2023), that R, T, and L tension and L compression can generally be omitted in plasticity models. However, considering compression only in the normal direction, as in Hassani et al. (2015), is insufficient, because rolling shear can yield plastic deformations that may be even larger and therefore must be included.

- **Viscoelasticity:** Models such as those by Fortino et al. (2009); Hassani et al. (2015); Yu et al. (2022) scale their creep compliances proportionally to the elastic compliance. However, the presented data reveal that this approach is invalid and that normalized creep is highly orthotropic. Furthermore, the moisture-dependence of creep is non-linear, unlike assumptions made by Hering and Niemz (2012), and cannot even be expressed by WLF equations, which were applied by Peng et al. (2022) on Chinese fir. In fact, normalized creep at 35% and 65% RH is constant across most orthotropic directions, whereas it increases rapidly at 90% RH, consistent with Hunt (1999). This could hint that creep might depend not only on the MC itself but also on the sorption mechanism.

- **Hygroexpansion:** Swelling and shrinkage in the R and T direction show a clear linear moisture dependence, similar to Neuhaus (1981). However, a piecewise linear fitting approach yields more accurate results for L hygroexpansion.

4.2 Reflections on the generality of results

To obtain samples from a comparable material across all campaigns, a single, regularly grown Norway spruce stem with fine annual ring structure was used. This allows for consistent comparison across all moisture-dependent parameters, but does not account for the statistical variation within and among trees. However, the obtained ratios and moisture scaling relations can be applied to expand sparse datasets from other trees. For cyclic loading, strength reduction is observed (Niemz and Sonderegger, 2017). As the plastic behavior is determined by incremental stress increase, such effects could potentially occur. However, for the small number of cycles below 30, the expected influence can be considered as minor, which is confirmed by above-average strength values. To improve strain measurement accuracy, future studies could employ 3D DIC (Jones and Iadicola, 2018). In particular, limited measurement accuracy for small-strain components led to large relative errors. Fortunately, these have only a small influence on the total absolute deformation because of their small magnitude. Additionally, the limited number of creep

test samples affects the statistical confidence of creep-related statements. This is more than compensated by the creep duration of 30 days. Hence, the time extrapolation is substantially improved relative to Hofer et al. (2019); Akter et al. (2022); Bengtsson et al. (2024), that tested only from 30 min to 24 h.

The data demonstrates that each rheological mechanism exhibits pronounced moisture-dependent orthotropy, which may be attributed to direction- and moisture-related deformation mechanisms on the cellular scale, such as bending, buckling, or stiffening of cell walls (Huang et al., 2020; Peng et al., 2022; Wang et al., 2025). Therefore, the strong influence of tissue structure limits the transferability of material parameters by density scaling between trees or even species. With the consistent moisture-scaling relations and parameter ratios provided through this work, one can expand the results from a limited number of tested directions and MCs to the entire orthotropic parameter space. For example, for plasticity, only R and T compression and rolling shear at a single MC need to be measured, whereas MC dependence arises from the moisture-scaling of strength. In general, the tests should ideally address the relevant and most dissimilar anatomical directions to minimize the expected error arising from parameter scaling. For creep behavior, one can identify groups of components that are most similar using clustering analysis. The results are presented in Tab. 2, enabling the identification of one relevant component per group. This approach enables adequate characterization of full creep orthotropy by a limited number of time-costly tests.

5 Conclusions

Based on the insights into the orthotropic behavior of wood provided in this work, several implications for future rheological models emerge to better capture its hygromechanical behavior. The completeness of the moisture states, strain contributions, and anatomical directions enabled the identification of consistent scaling parameters and basic simplifying assumptions related to orthotropic asymmetries and moisture dependencies. The most important implications from this study with respect to the current state of the art of wood models and parameter identification are:

- **Elasticity:** The moisture-dependency is best described by a quadratic function, thus measurements at three different MCs are necessary. Asymmetries between compression and tension, and between complementary shear planes, are less than 20 % and thus negligible. Furthermore, it is more accurate to measure the off-diagonal terms of the compliance matrix directly instead of the Poisson's ratios, which combine measurement errors from both the axial and lateral directions.

- **Plasticity:** The most pronounced plastic strains are observable for R and T compression and rolling shear, which should be respected in plasticity models. Here, moisture-dependent plasticity scales proportionally with moisture-dependent strength. This study confirms that strength decreases linearly with MC across the engineering-relevant moisture range, thereby requiring measurements at only two MCs. Furthermore, the shear strengths of the RL and LR planes are equal to those of the TL and LT planes, respectively, thereby reducing the number of required shear strength measurements.

- **Viscoelasticity:** The relation between the viscoelastic and the elastic compliance has negligible compression-tension and shear asymmetries, but is strongly orthotropic with up to one magnitude variation. This renders scaling with a single proportionality factor impossible. Furthermore, the moisture scaling is strongly orthotropic and particularly moisture-sensitive in the R, T, and rolling shear directions. For MCs below 12.5 %, creep remains generally proportional to the elastic compliance but increases at higher MCs, indicating that capillary condensation influences the creep mechanism. Consequently, moisture-dependent creep measurements are required for RH above 65 %. To reduce the number of required creep experiments in future studies, this paper identifies groups of the most dissimilar compliance components to be determined for a limited number of tests. The missing components can then be scaled using the parameter ratios from this study. The creep parameters are described with the time-moisture superposition principle (TMSP). The TMSP is suitable for describing wood creep but requires a modified time-shift function that deviates from the established WLF equation, which cannot account for different creep mechanisms across MCs. In this study, the utilized time-shift functions are purely empirical.

In future studies, the picture of the wood plasticity could be complemented by plastic deformation under biaxial stress states. Furthermore, to provide a physically motivated formulation of the creep time-shift functions, a more detailed investigation of creep across multiple moisture levels, from 12.5 % MC to fiber saturation, would be required. Negligible but detectable compression-tension asymmetries in creep suggest slight differences in creep mechanisms, which might be attributable to MC differences. Investigations of stress-dependent wood sorption may help clarify this, as the true MC may differ between stressed and stress-free wood. Finally, we address mechanosorptive creep in a follow-up study, employing the same samples and creep rack but with alternating RH.

Appendix

Tab. A1: Number of samples included in the material analysis. The values without brackets correspond to the compression tests and shear tests in the shear planes denoted in the table header, whereas the values in brackets correspond to the complementary tension and shear tests. For the lateral orientation ij, i denotes the force direction and j the strain direction.

	Parameter	**RH** [%]	**Sample Size**											
			axial			lateral						shear		
			R	T	L	RT	TR	RL	LR	TL	LT	RT	RL	TL
Scleronomic	Elasticity: $C_{0,ij}^{-1}$ (Eq. 2)	35	27	21	28	26	21	20	25	22	25	25	27	27
			(21)	(24)	(27)	(22)	(16)	(22)	(26)	(19)	(22)	(27)	(26)	(23)
		65	27	29	27	29	27	26	24	25	24	20	24	23
			(28)	(23)	(27)	(28)	(22)	(17)	(27)	(16)	(25)	(25)	(24)	(22)
		85	25	26	26	25	12	15	19	27	19	23	25	27
			(23)	(21)	(22)	(25)	(21)	(24)	(23)	(22)	(22)	(25)	(19)	(23)
		95	17	18	25	19	14	17	24	18	24	24	19	27
			(25)	(23)	(24)	(27)	(21)	(21)	(21)	(19)	(23)	(25)	(24)	(22)
	Strength: f_i	35	34	32	33	–	–	–	–	–	–	30	30	31
			(31)	(31)	(34)	–	–	–	–	–	–	(30)	(30)	(28)
		65	35	30	33	–	–	–	–	–	–	30	30	30
			(32)	(27)	(31)	–	–	–	–	–	–	(32)	(30)	(26)
		85	30	31	33	–	–	–	–	–	–	32	32	32
			(32)	(29)	(30)	–	–	–	–	–	–	(30)	(24)	(28)
		95	31	30	33	–	–	–	–	–	–	30	30	30
			(31)	(31)	(31)	–	–	–	–	–	–	(30)	(28)	(27)
	Plasticity: K_i, n_i (Eq. 4)	35	18	24	14	–	–	–	–	–	–	27	27	25
			(14)	(11)	(19)	–	–	–	–	–	–	(27)	(27)	(17)
		65	21	26	14	–	–	–	–	–	–	27	24	24
			(31)	(22)	(13)	–	–	–	–	–	–	(29)	(27)	(22)
		85	23	25	21	–	–	–	–	–	–	25	27	26
			(0)	(0)	(18)	–	–	–	–	–	–	(27)	(21)	(25)
		95	19	19	14	–	–	–	–	–	–	25	27	26
			(17)	(13)	(11)	–	–	–	–	–	–	(26)	(25)	(16)
Rheonomic	Viscoelasticity: $\boldsymbol{g}_{ij}$, $\boldsymbol{\tau}_{ij}$ (Eq. 6)	35	4	3	2	–	2	2	–	–	3	7	7	6
			(2)	(3)	(3)	–	(4)	(1)	–	–	(4)	(6)	(6)	(7)
		65	5	3	3	–	3	2	–	–	3	4	4	3
			(3)	(3)	(3)	–	(3)	(3)	–	–	(2)	(4)	(4)	(4)
		90	3	3	1	–	2	1	–	–	2	4	4	4
			(3)	(4)	(1)	–	(2)	(2)	–	–	(1)	(3)	(3)	(3)
Hygroresponsive	Sorption: $\omega(\varphi)$ (Eq. 10)	0-96	20											
	Hygroexpansion: α_i (Eq. 11)	0-96	10 (R), 10 (T), 10 (L)											
	Oven-dry density: ρ_0	0	62											

Tab. A2: Median settings of scleronomic tests, with sample count n, the camera resolution (AVT PIKE F-321B for 4 MP, VCXU-124M for 12.3 MP), image acquisition interval ΔT, loading rate $\dot{\sigma}$, lower and upper stresses of the first load cycle σ_{low} and σ_{up}, and their respective increment per load cycle $\Delta\sigma_{\mathrm{low}}$ and $\Delta\sigma_{\mathrm{up}}$. The type matches Fig. 1, with its lowercase letter indicating the loading type (compression c, shear s, tension t) and its uppercase letters the loading direction.

Type	**RH** [%]	n	**Resolution** [MP]	ΔT [s]	$\dot{\sigma}$ [MPa/s]	σ_{low} [MPa]	$\Delta\sigma_{\mathrm{low}}$ [MPa]	σ_{up} [MPa]	$\Delta\sigma_{\mathrm{up}}$ [MPa]
cL	**35**	30	4	2.0	0.76	20.21	1.26	30.31	1.26
	65	29	12.3	2.0	0.77	10.26	1.28	25.66	1.28
	85	29	4	2.0	0.78	2.59	1.30	10.37	1.30
	95	27	4	2.0	0.75	2.51	1.25	10.03	1.25
cR	**35**	28	4	2.0	0.30	1.02	0.00	3.55	0.10
	65	30	12.3	3.3	0.31	1.03	0.00	3.99	0.05
	85	27	4	2.0	0.31	1.02	0.00	1.83	0.10
	95	28	4	2.0	0.30	0.50	0.00	1.50	0.10
cT	**35**	26	4	2.0	0.30	1.01	0.00	2.03	0.25
	65	29	12.3	2.0	0.31	0.51	0.00	2.04	0.24
	85	28	4	2.0	0.30	0.50	0.00	1.51	0.25
	95	27	4	2.0	0.30	0.50	0.00	1.24	0.25
sLR	**35**	27	12.3	2.0	0.28	0.28	0.00	0.56	0.56
	65	26	12.3	2.0	0.28	0.28	0.00	0.55	0.55
	85	21	12.3	1.0	0.28	0.28	0.00	0.56	0.56
	95	25	12.3	1.0	0.27	0.27	0.00	0.55	0.55
sLT	**35**	25	12.3	2.0	0.28	0.28	0.00	0.56	0.56
	65	22	12.3	2.0	0.27	0.27	0.00	0.55	0.55
	85	25	12.3	1.0	0.28	0.28	0.00	0.56	0.56
	95	23	12.3	1.0	0.27	0.27	0.00	0.54	0.54
sRL	**35**	27	12.3	2.0	0.14	0.28	0.00	0.55	0.55
	65	26	12.3	2.0	0.14	0.28	0.00	0.55	0.55
	85	27	12.3	1.5	0.13	0.28	0.00	0.54	0.54
	95	27	12.3	1.5	0.14	0.27	0.00	0.55	0.28
sRT	**35**	27	12.3	2.0	0.07	0.27	0.00	0.40	0.13
	65	27	12.3	2.0	0.07	0.27	0.00	0.41	0.14
	85	27	12.3	1.0	0.07	0.28	0.00	0.41	0.14
	95	27	12.3	1.5	0.07	0.28	0.00	0.42	0.14
sTL	**35**	27	12.3	2.0	0.14	0.28	0.00	0.54	0.54
	65	25	12.3	2.0	0.14	0.28	0.00	0.55	0.55
	85	27	12.3	1.5	0.13	0.28	0.00	0.54	0.54
	95	27	12.3	1.5	0.14	0.27	0.00	0.55	0.28
sTR	**35**	27	12.3	2.0	0.05	0.22	0.00	0.32	0.11
	65	27	12.3	2.0	0.07	0.27	0.00	0.41	0.14
	85	27	12.3	1.0	0.05	0.22	0.00	0.32	0.11
	95	27	12.3	1.0	0.05	0.22	0.00	0.33	0.11
tL	**35**	20	12.3	2.0	1.97	13.12	9.84	32.79	16.40
	65	24	12.3	2.0	2.08	8.32	8.32	33.26	16.63
	85	24	4	1.5	2.03	8.10	4.05	32.41	16.20
	95	25	4	2.0	2.00	8.00	4.00	32.02	15.99
tR	**35**	28	4	2.0	0.31	0.51	0.00	2.31	0.26
	65	33	12.3	2.0	0.31	1.03	0.00	2.31	0.26
	85	29	4	1.3	0.30	0.50	0.00	1.77	0.25
	95	28	4	1.0	0.30	0.50	0.00	1.76	0.25
tT	**35**	27	4	1.0	0.31	0.51	0.00	1.54	0.26
	65	24	12.3	2.0	0.31	1.02	0.00	1.78	0.25
	85	26	4	1.0	0.30	0.51	0.00	1.77	0.25
	95	27	4	1.0	0.30	0.50	0.00	1.63	0.13

Tab. A3: Fitting parameters of elastic stiffness $(1/C_0^{-1})(\omega) = p_0\omega^2 + p_1$ [MPa] (ω given in %) matching to Fig. 4.

Component	$\boldsymbol{p_0}$	$\boldsymbol{p_1}$	$\boldsymbol{R^2}$
$E_{c,R}$	-1.2164 ± 0.0760	1291.25 ± 19.57	0.73
$E_{t,R}$	-1.1178 ± 0.0628	1266.66 ± 17.62	0.77
$E_{c,R} \cup E_{t,R}$	-1.1687 ± 0.0490	1280.04 ± 13.19	0.75
$E_{c,T}$	-0.4470 ± 0.0394	693.87 ± 10.93	0.58
$E_{t,T}$	-0.4717 ± 0.0342	776.57 ± 9.94	0.68
$E_{c,T} \cup E_{t,T}$	-0.4484 ± 0.0316	731.93 ± 8.98	0.52
$E_{c,L}$	-4.9153 ± 0.7291	$13\,143.20 \pm 212.97$	0.30
$E_{t,L}$	-4.3928 ± 0.8028	$15\,099.10 \pm 261.43$	0.23
$E_{c,L} \cup E_{t,L}$	-4.1716 ± 0.6761	$13\,972.72 \pm 208.81$	0.16
G_{RT}	-0.0173 ± 0.0032	57.33 ± 1.12	0.24
G_{TR}	-0.0198 ± 0.0032	53.44 ± 1.04	0.28
$G_{RT} \cup G_{TR}$	-0.0181 ± 0.0024	55.16 ± 0.82	0.23
G_{RL}	-0.9886 ± 0.0679	1440.97 ± 21.48	0.69
G_{LR}	-1.0141 ± 0.0696	1575.70 ± 21.56	0.70
$G_{RL} \cup G_{LR}$	-0.9967 ± 0.0563	1506.38 ± 17.63	0.63
G_{TL}	-1.2639 ± 0.1090	1786.68 ± 38.42	0.57
G_{LT}	-1.4204 ± 0.0860	1727.27 ± 27.52	0.76
$G_{TL} \cup G_{LT}$	-1.3058 ± 0.0758	1750.87 ± 25.59	0.61
$K_{c,RT}$	-2.9710 ± 0.1919	2688.08 ± 49.86	0.58
$K_{t,RT}$	-2.9872 ± 0.1299	2708.69 ± 37.84	0.75
$K_{c,RT} \cup E_{t,RT}$	-2.9720 ± 0.1140	2696.82 ± 31.51	0.66
$K_{c,RL}$	5.4593 ± 9.9187	$31\,639.37 \pm 2794.34$	0.00
$K_{t,RL}$	-19.2734 ± 4.8115	$25\,945.99 \pm 1456.47$	0.08
$K_{c,RL} \cup E_{t,RL}$	-9.9158 ± 5.7248	$29\,169.71 \pm 1675.84$	0.01
$K_{c,TL}$	-7.4562 ± 17.2374	$27\,942.64 \pm 4927.79$	0.00
$K_{t,TL}$	-16.8980 ± 4.2044	$20\,387.97 \pm 1333.83$	0.09
$K_{c,TL} \cup E_{t,TL}$	-14.9514 ± 9.2124	$25\,056.28 \pm 2773.71$	0.01

Tab. A4: Fitting parameters of strength $|f_{\max}(\omega)| = p_0\omega + p_1$ [MPa] (ω given in %) matching to Fig. 6.

Component	$\boldsymbol{p_0}$	$\boldsymbol{p_1}$	$\boldsymbol{R^2}$
$f_{c,R}$	-0.121 ± 0.007	5.96 ± 0.11	0.84
$f_{t,R}$	-0.175 ± 0.012	8.16 ± 0.18	0.65
$f_{c,R} \cup f_{t,R}$	-0.152 ± 0.009	7.29 ± 0.14	0.53
$f_{c,T}$	-0.194 ± 0.008	8.41 ± 0.12	0.84
$f_{t,T}$	-0.107 ± 0.013	5.76 ± 0.21	0.41
$f_{c,T} \cup f_{t,T}$	-0.165 ± 0.011	7.37 ± 0.18	0.48
$f_{c,L}$	-1.872 ± 0.061	67.18 ± 0.96	0.88
$f_{t,L}$	-1.600 ± 0.373	153.87 ± 6.52	0.17
$f_{c,L} \cup f_{t,L}$	-0.468 ± 0.557	83.47 ± 9.20	0.00
$f_{s,RT}$	-0.008 ± 0.002	1.43 ± 0.04	0.09
$f_{s,TR}$	-0.022 ± 0.003	2.20 ± 0.05	0.33
$f_{s,RT} \cup f_{s,TR}$	-0.015 ± 0.004	1.82 ± 0.06	0.06
$f_{s,RL}$	-0.182 ± 0.011	8.20 ± 0.19	0.77
$f_{s,LR}$	-0.195 ± 0.013	10.47 ± 0.22	0.68
$f_{s,RL} \cup f_{s,LR}$	-0.203 ± 0.017	9.71 ± 0.28	0.44
$f_{s,TL}$	-0.188 ± 0.014	8.78 ± 0.24	0.72
$f_{s,LT}$	-0.189 ± 0.015	10.12 ± 0.26	0.59
$f_{s,TL} \cup f_{s,LT}$	-0.189 ± 0.014	9.59 ± 0.24	0.50

Tab. A5: Fitting parameters of plastic hardening $\sigma(\epsilon_{\mathrm{pl}}, \omega) = \epsilon_{\mathrm{pl}}^{1/n} K f_{\max}(\omega)$ [MPa] matching to Fig. 8 and Tab. A4.

Component	$\boldsymbol{K}$	$\boldsymbol{n}$	$\boldsymbol{R^2}$
$\sigma_{c,R}$	1.111 ± 0.014	43.917 ± 5.257	0.95
$\sigma_{t,R}$	2.699 ± 0.430	6.115 ± 0.776	0.80
$\sigma_{c,T}$	1.803 ± 0.112	7.977 ± 0.729	0.97
$\sigma_{t,T}$	5.940 ± 1.577	3.923 ± 0.477	0.90
$\sigma_{c,L}$	1.952 ± 0.202	10.752 ± 1.497	0.97
$\sigma_{t,L}$	4.685 ± 1.275	4.072 ± 0.605	0.83
$\sigma_{s,RT}$	2.797 ± 0.171	4.272 ± 0.177	0.98
$\sigma_{s,TR}$	2.043 ± 0.103	4.600 ± 0.217	0.99
$\sigma_{s,RL}$	3.258 ± 0.428	5.958 ± 0.560	0.94
$\sigma_{s,LR}$	2.928 ± 0.271	6.228 ± 0.437	0.99
$\sigma_{s,TL}$	2.435 ± 0.306	7.746 ± 0.907	0.98
$\sigma_{s,LT}$	2.970 ± 0.288	6.728 ± 0.513	0.96

Tab. A6: Fitting parameters of master creep curve $C_{\mathrm{ve}}^{-1}(t, \omega)/C_0^{-1}(\omega) = \sum_{k=1}^{n} g_k(1 - \mathrm{e}^{-(a_\omega(\omega)t)/\tau_k})$ [-] matching to Fig. 11a and the time shift function $a_\omega(\omega)$ in Tab. A7.

Component	$\boldsymbol{k}$	$\boldsymbol{\tau_k}$	$\boldsymbol{g_k}$	$\boldsymbol{R^2}$
$E_{c,R}$	0	$(1.408 \pm 0.507) \times 10^3$	0.214 ± 0.016	0.98
	1	$(8.804 \pm 2.287) \times 10^4$	0.233 ± 0.038	
	2	$(6.123 \pm 1.050) \times 10^5$	0.386 ± 0.035	
	3	$(1.242 \pm 0.052) \times 10^7$	1.894 ± 0.023	
$E_{t,R}$	0	$(8.500 \pm 8.672) \times 10^1$	0.272 ± 0.010	0.99
	1	$(1.046 \pm 0.199) \times 10^6$	0.337 ± 0.039	
	2	$(1.513 \pm 0.400) \times 10^7$	0.472 ± 0.059	
	3	$(1.522 \pm 0.197) \times 10^8$	1.244 ± 0.068	
	4	$(0.440 \pm 1.068) \times 10^{10}$	2.316 ± 1.268	
$E_{c,R} \cup E_{t,R}$	0	$(5.329 \pm 2.080) \times 10^2$	0.236 ± 0.009	0.98
	1	$(1.870 \pm 0.292) \times 10^5$	0.275 ± 0.026	
	2	$(1.768 \pm 0.251) \times 10^6$	0.424 ± 0.025	
	3	$(2.715 \pm 0.178) \times 10^7$	1.406 ± 0.045	
	4	$(8.804 \pm 5.852) \times 10^8$	2.265 ± 1.046	
$E_{c,T}$	0	$(1.346 \pm 0.480) \times 10^3$	0.413 ± 0.028	0.96
	1	$(1.347 \pm 0.203) \times 10^5$	0.529 ± 0.040	
	2	$(1.733 \pm 0.262) \times 10^6$	0.993 ± 0.083	
	3	$(0.575 \pm 1.259) \times 10^8$	2.488 ± 2.670	
$E_{t,T}$	0	$(1.506 \pm 0.660) \times 10^2$	0.382 ± 0.018	0.99
	1	$(8.090 \pm 2.675) \times 10^4$	0.241 ± 0.039	
	2	$(1.122 \pm 0.197) \times 10^6$	0.505 ± 0.038	
	3	$(3.421 \pm 0.329) \times 10^7$	1.415 ± 0.099	
	4	$(3.637 \pm 1.238) \times 10^8$	1.359 ± 0.122	
$E_{c,T} \cup E_{t,T}$	0	$(4.236 \pm 4.536) \times 10^1$	0.281 ± 0.034	0.97
	1	$(7.327 \pm 2.822) \times 10^3$	0.202 ± 0.035	
	2	$(3.279 \pm 0.353) \times 10^5$	0.545 ± 0.026	
	3	$(4.948 \pm 0.517) \times 10^6$	0.822 ± 0.041	
	4	$(5.690 \pm 0.405) \times 10^7$	1.711 ± 0.038	

Tab. A6 (continued)

Component	k	τ_k	g_k	R^2
$E_{c,L}$	0	$(1.096 \pm 0.328) \times 10^4$	0.104 ± 0.015	0.78
	1	$(1.779 \pm 0.696) \times 10^5$	0.099 ± 0.016	
	2	$(3.061 \pm 0.862) \times 10^6$	0.178 ± 0.015	
$E_{t,L}$	0	$(2.326 \pm 0.365) \times 10^4$	0.090 ± 0.003	0.75
	1	$(4.397 \pm 0.503) \times 10^6$	0.130 ± 0.005	
$E_{c,L} \cup E_{t,L}$	0	$(0.869 \pm 6.544) \times 10^{-1}$	0.015 ± 0.005	0.79
	1	$(2.112 \pm 0.495) \times 10^4$	0.075 ± 0.006	
	2	$(9.378 \pm 1.817) \times 10^5$	0.108 ± 0.010	
	3	$(1.975 \pm 0.507) \times 10^7$	0.197 ± 0.016	
G_{RT}	0	$(4.121 \pm 1.232) \times 10^2$	0.161 ± 0.007	0.99
	1	$(4.748 \pm 0.777) \times 10^4$	0.117 ± 0.008	
	2	$(4.328 \pm 0.319) \times 10^6$	0.257 ± 0.007	
	3	$(2.988 \pm 0.282) \times 10^8$	0.392 ± 0.013	
	4	$(7.857 \pm 0.512) \times 10^9$	0.670 ± 0.018	
	5	$(1.792 \pm 0.604) \times 10^{11}$	0.257 ± 0.029	
G_{TR}	0	$(2.181 \pm 0.634) \times 10^2$	0.168 ± 0.008	0.99
	1	$(4.154 \pm 0.964) \times 10^4$	0.089 ± 0.009	
	2	$(1.125 \pm 0.099) \times 10^6$	0.217 ± 0.008	
	3	$(4.069 \pm 0.365) \times 10^7$	0.409 ± 0.012	
	4	$(1.148 \pm 0.093) \times 10^9$	0.777 ± 0.042	
	5	$(1.574 \pm 1.640) \times 10^{10}$	0.282 ± 0.113	
$G_{RT} \cup G_{TR}$	0	$(2.577 \pm 0.607) \times 10^2$	0.159 ± 0.005	0.99
	1	$(3.934 \pm 0.527) \times 10^4$	0.107 ± 0.006	
	2	$(2.024 \pm 0.114) \times 10^6$	0.242 ± 0.005	
	3	$(1.100 \pm 0.076) \times 10^8$	0.396 ± 0.009	
	4	$(3.110 \pm 0.169) \times 10^9$	0.700 ± 0.020	
	5	$(3.534 \pm 0.904) \times 10^{10}$	0.226 ± 0.017	
G_{RL}	0	$(5.978 \pm 1.183) \times 10^2$	0.208 ± 0.004	0.95
	1	$(2.839 \pm 0.443) \times 10^5$	0.149 ± 0.019	
	2	$(2.214 \pm 0.639) \times 10^6$	0.221 ± 0.034	
	3	$(5.619 \pm 4.113) \times 10^7$	1.211 ± 0.787	
G_{LR}	0	$(5.644 \pm 3.156) \times 10^2$	0.092 ± 0.010	0.93
	1	$(2.764 \pm 0.410) \times 10^4$	0.154 ± 0.010	
	2	$(1.102 \pm 0.135) \times 10^6$	0.187 ± 0.011	
	3	$(2.134 \pm 0.202) \times 10^7$	0.515 ± 0.015	
$G_{RL} \cup G_{LR}$	0	$(5.828 \pm 1.672) \times 10^2$	0.121 ± 0.009	0.94
	1	$(1.837 \pm 0.307) \times 10^4$	0.111 ± 0.009	
	2	$(5.624 \pm 0.704) \times 10^5$	0.166 ± 0.014	
	3	$(5.985 \pm 2.065) \times 10^6$	0.274 ± 0.085	
	4	$(1.041 \pm 2.151) \times 10^8$	0.879 ± 1.151	
G_{TL}	0	$(1.428 \pm 1.037) \times 10^3$	0.076 ± 0.022	0.94
	1	$(2.348 \pm 0.512) \times 10^4$	0.176 ± 0.021	
	2	$(1.039 \pm 0.353) \times 10^6$	0.183 ± 0.063	
	3	$(5.941 \pm 3.313) \times 10^6$	0.224 ± 0.050	
	4	$(7.428 \pm 1.810) \times 10^7$	0.755 ± 0.042	

Tab. A6 (continued)

Component	k	τ_k	g_k	R^2
G_{LT}	0	$(7.323 \pm 2.917) \times 10^2$	0.115 ± 0.009	0.95
	1	$(4.152 \pm 1.030) \times 10^4$	0.126 ± 0.016	
	2	$(4.208 \pm 0.897) \times 10^5$	0.148 ± 0.014	
	3	$(9.018 \pm 2.771) \times 10^6$	0.344 ± 0.124	
	4	$(4.408 \pm 1.797) \times 10^7$	0.453 ± 0.105	
$G_{TL} \cup G_{LT}$	0	$(1.065 \pm 0.404) \times 10^3$	0.096 ± 0.010	0.94
	1	$(3.225 \pm 0.500) \times 10^4$	0.153 ± 0.011	
	2	$(6.768 \pm 1.176) \times 10^5$	0.156 ± 0.014	
	3	$(7.934 \pm 1.799) \times 10^6$	0.316 ± 0.048	
	4	$(6.857 \pm 1.738) \times 10^7$	0.612 ± 0.033	
$\frac{\nu_{c,TR}}{E_{c,T}}$	0	$(6.489 \pm 8.399) \times 10^3$	0.080 ± 0.031	0.98
	1	$(2.553 \pm 0.401) \times 10^5$	0.476 ± 0.031	
	2	$(2.742 \pm 0.266) \times 10^7$	1.875 ± 0.158	
	3	$(0.674 \pm 1.476) \times 10^9$	1.845 ± 2.807	
$\frac{\nu_{t,TR}}{E_{t,T}}$	0	$(4.055 \pm 2.606) \times 10^3$	0.141 ± 0.025	0.95
	1	$(3.530 \pm 0.973) \times 10^5$	0.529 ± 0.095	
	2	$(3.217 \pm 1.991) \times 10^6$	0.437 ± 0.131	
	3	$(2.562 \pm 0.491) \times 10^7$	1.702 ± 0.119	
$\frac{\nu_{c,TR}}{E_{c,T}} \cup \frac{\nu_{t,TR}}{E_{t,T}}$	0	$(4.742 \pm 3.005) \times 10^3$	0.116 ± 0.024	0.96
	1	$(2.111 \pm 0.623) \times 10^5$	0.396 ± 0.071	
	2	$(1.896 \pm 1.274) \times 10^6$	0.257 ± 0.076	
	3	$(2.002 \pm 0.425) \times 10^7$	1.493 ± 0.194	
	4	$(0.445 \pm 1.019) \times 10^9$	2.332 ± 3.679	
$\frac{\nu_{c,RL}}{E_{c,R}}$	0	$(1.130 \pm 0.462) \times 10^4$	1.163 ± 0.253	0.81
	1	$(1.587 \pm 0.558) \times 10^5$	1.518 ± 0.235	
	2	$(4.409 \pm 0.818) \times 10^6$	2.286 ± 0.157	
$\frac{\nu_{t,RL}}{E_{t,R}}$	0	$(4.370 \pm 0.742) \times 10^5$	1.413 ± 0.143	0.70
	1	$(1.331 \pm 0.707) \times 10^7$	1.985 ± 0.454	
$\frac{\nu_{c,RL}}{E_{c,R}} \cup \frac{\nu_{t,RL}}{E_{t,R}}$	0	$(3.496 \pm 0.893) \times 10^4$	0.883 ± 0.097	0.85
	1	$(1.016 \pm 0.217) \times 10^6$	1.504 ± 0.136	
	2	$(1.953 \pm 0.298) \times 10^7$	2.601 ± 0.136	
$\frac{\nu_{c,LT}}{E_{c,L}}$	0	$(1.472 \pm 0.227) \times 10^5$	0.446 ± 0.022	0.99
	1	$(2.461 \pm 0.486) \times 10^7$	0.773 ± 0.083	
	2	$(3.414 \pm 0.125) \times 10^8$	4.853 ± 0.079	
$\frac{\nu_{t,LT}}{E_{t,L}}$	0	$(1.784 \pm 0.184) \times 10^5$	0.262 ± 0.010	0.93
	1	$(2.306 \pm 0.147) \times 10^7$	1.432 ± 0.040	
$\frac{\nu_{c,LT}}{E_{c,L}} \cup \frac{\nu_{t,LT}}{E_{t,L}}$	0	$(1.402 \pm 0.176) \times 10^5$	0.313 ± 0.016	0.99
	1	$(8.714 \pm 1.779) \times 10^6$	0.490 ± 0.059	
	2	$(1.596 \pm 0.680) \times 10^8$	1.307 ± 0.755	
	3	$(5.151 \pm 0.703) \times 10^8$	4.000 ± 2.830	

Tab. A7: Fitting parameters of time shift function $\ln(a_\omega(\omega)) = p_0 + (\ln(a_R) - p_0)/(1 + \exp(p_1 - \omega))$ [ln(s)] matching to Fig. 11b and the master creep curves in Tab. A6.

Component	p_0	p_1	$\ln(a_R)$	R^2
$E_{c,R}$	17.483 ± 1.400	-0.020 ± 0.270	2.928	0.71
$E_{t,R}$	17.190 ± 1.851	-0.066 ± 0.792	7.209	0.82
$E_{c,R} \cup E_{t,R}$	18.345 ± 0.586	-0.016 ± 0.384	5.603	0.69
$E_{c,T}$	18.762 ± 1.261	-0.005 ± 0.456	2.577	0.45
$E_{t,T}$	17.003 ± 2.205	-0.064 ± 0.743	5.810	0.74
$E_{c,T} \cup E_{t,T}$	18.426 ± 0.695	-0.013 ± 0.460	4.895	0.58
$E_{c,L}$	12.791 ± 0.528	-1.350 ± 0.446	1.806	0.83
$E_{t,L}$	17.642 ± 6.497	-0.021 ± 1.112	3.553	0.22
$E_{c,L} \cup E_{t,L}$	19.378 ± 1.912	-0.004 ± 0.706	3.543	0.09
G_{RT}	18.356 ± 0.642	-0.035 ± 0.843	12.390	0.74
G_{TR}	17.976 ± 0.703	-0.041 ± 0.594	9.827	0.79
$G_{RT} \cup G_{TR}$	18.276 ± 0.427	-0.035 ± 0.499	11.507	0.76
G_{RL}	19.094 ± 0.861	-0.003 ± 0.278	2.467	0.42
G_{LR}	19.321 ± 1.113	-0.004 ± 0.533	3.701	0.21
$G_{RL} \cup G_{LR}$	19.255 ± 0.701	-0.004 ± 0.290	3.129	0.28
G_{TL}	19.117 ± 0.542	-0.006 ± 0.355	4.371	0.61
G_{LT}	18.525 ± 0.810	-0.010 ± 0.334	4.169	0.59
$G_{TL} \cup G_{LT}$	19.015 ± 0.394	-0.007 ± 0.232	4.478	0.60
$\frac{\nu_{c,TR}}{E_{c,T}}$	17.018 ± 2.759	-0.056 ± 0.691	5.087	0.75
$\frac{\nu_{t,TR}}{E_{t,T}}$	17.570 ± 3.709	-0.024 ± 0.899	3.880	0.32
$\frac{\nu_{c,TR}}{E_{c,T}} \cup \frac{\nu_{t,TR}}{E_{t,T}}$	17.519 ± 1.891	-0.031 ± 0.580	4.719	0.49
$\frac{\nu_{c,RL}}{E_{c,R}}$	17.309 ± 5.805	-0.027 ± 0.890	3.339	0.49
$\frac{\nu_{t,RL}}{E_{t,R}}$	10.000 ± 2.194	-2.140 ± 3.381	0.176	0.22
$\frac{\nu_{c,RL}}{E_{c,R}} \cup \frac{\nu_{t,RL}}{E_{t,R}}$	20.000 ± 0.378	-0.003 ± 1.128	4.954	-0.13
$\frac{\nu_{c,LT}}{E_{c,L}}$	17.037 ± 3.764	-0.074 ± 0.932	6.913	0.71
$\frac{\nu_{t,LT}}{E_{t,L}}$	17.724 ± 12.434	-0.007 ± 0.772	1.225	0.07
$\frac{\nu_{c,LT}}{E_{c,L}} \cup \frac{\nu_{t,LT}}{E_{t,L}}$	18.950 ± 0.883	-0.011 ± 0.665	7.143	0.48

Acknowledgements: The contribution to this work by Phison Sisuwan and Thomas Schnider for sample preparation, as well as the financial support from the Swiss National Science Foundation under SNF grant 200021_192186 "Creep behavior of wood on multiple scales", is highly appreciated.

Data availability: A Git repository (Maas and Wittel, 2026) provides the whole dataset via Python Jupyter notebooks. The notebooks include interactive widgets for exploring the data and exporting the desired parts. The repository's README file provides detailed information on its usage. The available data comprise the experimental data points and fitting models of all figures used in this study.

Contributions: *J.M.M.* contributed to Methodology, Software, Validation, Formal analysis, Investigation, Data Curation, Writing – Original Draft, Visualization. *F.K.W.* contributed to Conceptualization, Methodology, Resources, Writing – Review & Editing, Supervision, Project administration, Funding acquisition.

References

Adalian, C. and Morlier, P. (2002). "WOOD MODEL" for the dynamic behaviour of wood in multiaxial compression. *Holz Roh- Werkst.* 60 (6): 433–439.

Akter, S. T. and Bader, T. K. (2020). Experimental assessment of failure criteria for the interaction of normal stress perpendicular to the grain with rolling shear stress in Norway spruce clear wood. *Eur. J. Wood Prod.* 78 (6): 1105–1123.

Akter, S. T., Binder, E., and Bader, T. K. (2022). Moisture and short-term time-dependent behavior of Norway spruce clear wood under compression perpendicular to the grain and rolling shear. *Wood Mater. Sci. Eng.* 18 (2): 580–593.

Al-musawi, H., Matz, P., Jakob, M., Halbauer, P., Krenke, T., and Müller, U. (2024). Stress–strain behaviour of wood in compression: Experimental and analytical investigations. *Results Eng.* 24: 103616.

Amando de Barros, J. O. and Wittel, F. K. (2024). Unifying model for the rheological behavior of hygroresponsive materials. *Phys. Rev. E* 109 (4): 044139.

Bachtiar, E. V., Sanabria, S. J., Mittig, J. P., and Niemz, P. (2017). Moisture-dependent elastic characteristics of walnut and cherry wood by means of mechanical and ultrasonic test incorporating three different ultrasound data evaluation techniques. *Wood Sci. Technol.* 51 (1): 47–67.

Bengtsson, R., Bergeron, L., Afshar, R., Mousavi, M., and Gamstedt, E. K. (2024). Evaluating the viscoelastic shear properties of clear wood via off-axis compression testing and digital-image correlation. *Mech. Time-Depend. Mater.* 28: 2069–2083.

Benvenuti, E., Orlando, N., Gebhardt, C., and Kaliske, M. (2020). An orthotropic multi-surface damage-plasticity FE-formulation for wood: Part II – Numerical applications. *Computers & Structures* 240: 106351.

Blaber, J., Adair, B., and Antoniou, A. (2015). Ncorr: Open-Source 2D Digital Image Correlation Matlab Software. *Exp. Mech.* 55 (6): 1105–1122.

Bodig, J. and Jayne, B. A. (1982). *Mechanics of Wood and Wood Composites*. Van Nostrand Reinhold, New York.

Cariou, J.-L. (1987). *Caractérisation d'un matériau viscoélastique anisotrope: le bois*. PhD thesis. Talence, Université Bordeaux 1.

Dahl, K. B. and Malo, K. A. (2009a). Linear shear properties of spruce softwood. *Wood Sci. Technol.* 43 (5–6): 499–525a.

Dahl, K. B. and Malo, K. A. (2009b). Nonlinear shear properties of spruce softwood: Experimental results. *Wood Sci.Technol.* 43 (7-8): 539–558b.

Dent, R. W. (1977). A Multilayer Theory for Gas Sorption: Part I: Sorption of a Single Gas. *Text. Res. J.* 47 (2): 145–152.

DIN 52182 (1976). Prüfung von Holz: Bestimmung der Rohdichte. Standard, German Institute for Standardization.

DIN 52188 (1979). Prüfung von Holz: Bestimmung der Zugfestigkeit parallel zur Faser. Standard, German Institute for Standardization.

DIN 52192 (1979). Prüfung von Holz: Druckversuch quer zur Faserrichtung. Standard, German Institute for Standardization.

DIN EN 13183-1 (2002). Feuchtegehalt eines Stückes Schnittholz – Bestimmung durch Darrverfahren. Standard, German Institute for Standardization.

Dumail, J.-F., Olofsson, K., and Salmén, L. (2000). An Analysis of Rolling Shear of Spruce Wood by the Iosipescu Method. *Holzforschung* 54 (4): 420–426.

Eberhardsteiner, J. (2002). *Mechanisches Verhalten von Fichtenholz: Experimentelle Bestimmung der biaxialen Festigkeitseigenschaften*, 1 ed. Springer-Verlag Wien GmbH, Vienna.

Ferrara, A., Amando de Barros, J. O., Koch, S. M., and Wittel, F. K. (2025). Morphologic evolution in simulated wood densification. *Wood Sci. Technol.* 59 (5): 91.

Ferrara, A. and Wittel, F. K. (2024). Micro-mechanical tests on tissue slices of Norway spruce: Tensile and shear performance. *Holzforschung* 78 (11-12): 624–630.

Ferrara, A. and Wittel, F. K. (2025). Tensile creep of Norway spruce on the tissue scale. *Mech. Time-Depend. Mater.* 29 (2): 36.

Fleischmann, M. (2005). *Numerische Berechnung von Holzkonstruktionen unter Verwendung eines realitätsnahen orthotropen elasto-plastischen Werkstoffmodells*. PhD thesis. Vienna, Vienna University of Technology.

Fortino, S., Mirianon, F., and Toratti, T. (2009). A 3D moisture-stress FEM analysis for time dependent problems in timber structures. *Mech. Time-Depend. Mater.* 13 (4): 333–356.

Gerhards, C. C. (1982). Effect of Moisture Content and Temperature on the Mechanical Properties of Wood: An Analysis of Immediate Effects. *Wood Fiber Sci.* 14 (1): 4–36.

Greenspan, L. (1977). Humidity Fixed Points of Binary Saturated Aqueous Solutions. *J. Res. Natl. Bur. Stand. A Phys. Chem.* 81A: 89–96.

Gressel, P. (1983). Erfassung, systematische Auswertung und Ergänzung bisheriger Untersuchungen über das rheologische Verhalten von Holz und Holzwerkstoffen - Ein Beitrag zur Verbesserung des Formänderungsnachweises nach DIN 1052 "Holzbauwerke". Abschlussbericht AIF 4289, AIF 5348, Versuchsanstalt für Stahl, Holz und Steine, Abt. Ingenieurholzbau, Universität Fridericiana Karlsruhe.

Gressel, P. (1984). Zur vorhersage des langfristigen formänderungsverhaltens aus kurzkriechversuchen. *Holz Roh. Werkst.* 42 (8): 293–301.

Gutierrez-Lemini, D. (2014). *Engineering Viscoelasticity*. Springer US, Boston, MA.

Hailwood, A. J. and Horrobin, S. (1946). Absorption of water by polymers: analysis in terms of a simple model. *Trans. Faraday Soc.* 42: 84–92.

Hajikarimi, P. and Moghadas Nejad, F. (2021). *Applications of Viscoelasticity*, 1 ed. Elsevier, Amsterdam, Netherlands.

Hajikarimi, P., Moghadas Nejad, F., and Mohammadi Aghdam, M. (2018). Implementing General Power Law to Interconvert Linear Viscoelastic Functions of Modified Asphalt Binders. *J. Transp. Eng. B: Pavements* 144 (2): 04018010.

Hanhijärvi, A. and Mackenzie-Helnwein, P. (2003). Computational Analysis of Quality Reduction during Drying of Lumber due to Irrecoverable Deformation. I: Orthotropic Viscoelastic-Mechanosorptive-Plastic Material Model for the Transverse Plane of Wood. *J. Eng. Mech.* 129 (9): 996–1005.

Hansen, K. K. (1986). *Sorption Isotherms: A Catalogue*. Byg Rapport. Technical University of Denmark.

Hassani, M. M., Wittel, F. K., Hering, S., and Herrmann, H. J. (2015). Rheological model for wood. *Comput. Methods Appl. Mech. Eng.* 283 (Supplement C): 1032–1060.

Hayashi, K., Felix, B., and Le Govic, C. (1993). Wood viscoelastic compliance determination with special attention to measurement problems. *Mater. Struct.* 26 (6): 370–376.

Hering, S., Keunecke, D., and Niemz, P. (2012a). Moisture-dependent orthotropic elasticity of beech wood. *Wood Sci. Technol.* 46 (5): 927–938a.

Hering, S. and Niemz, P. (2012). Moisture-dependent, viscoelastic creep of European beech wood in longitudinal direction. *Eur. J. Wood Prod.* 70 (5): 667–670.

Hering, S., Saft, S., Resch, E., Niemz, P., and Kaliske, M. (2012b). Characterisation of moisture-dependent plasticity of beech wood and its application to a multi-surface plasticity model. *Holzforschung* 66 (3): 373–380b.

Hofer, U., Pichler, C., Maderebner, R., and Lackner, R. (2019). Lomnitz-type viscoelastic behavior of clear spruce wood as identified by creep and relaxation experiments: Influence of moisture content and elevated temperatures up to 80 °C. *Wood Sci. Technol.* 53 (4): 765–783.

Huang, C., Gong, M., Chui, Y., and Chan, F. (2020). Mechanical behaviour of wood compressed in radial direction-part I. New method of determining the yield stress of wood on the stress-strain curve. *J. Bioresour. Bioprod.* 5 (3): 186–195.

Hunt, D. G. (1999). A Unified Approach to Creep of Wood. *Proc. Math. Phys. Eng. Sci.* 455 (1991): 4077–4095.

Jiang, J., Bachtiar, E. V., Lu, J., and Niemz, P. (2017). Moisture-dependent orthotropic elasticity and strength properties of Chinese fir wood. *Eur. J. Wood Prod.* 75 (6): 927–938.

Jones, E. and Iadicola, M. (2018). A Good Practices Guide for Digital Image Correlation. Technical report, International Digital Image Correlation Society.

Kaliske, M., Jenkel, C., Saft, S., and Resch, E. (2010). Computational Models for Wooden Structures. *Comput. Technol. Rev.* 2: 145–176.

Kê, T.-S. (1947). Experimental Evidence of the Viscous Behavior of Grain Boundaries in Metals. *Phys. Rev.* 71 (8): 533–546.

Keunecke, D., Hering, S., and Niemz, P. (2008). Three-dimensional elastic behaviour of common yew and Norway spruce. *Wood Sci. Technol.* 42 (8): 633–647.

Kienzler, R. and Schröder, R. (2019). *Einführung in die Höhere Festigkeitslehre*. Springer Vieweg Berlin, Heidelberg.

Knigge, W. and Schulz, H. (1966). *Grundriss der Forstbenutzung : Entstehung, Eigenschaften, Verwertung und Verwendung des Holzes und anderer Forstprodukte*. Paul Parey, Hamburg.

Kollmann, F. F. and Côté, W. A. (1968). *Principles of Wood Science and Technology I Solid Wood*, 1 ed. Springer-Verlag Berlin Heidelberg.

Kumpenza, C., Matz, P., Halbauer, P., Grabner, M., Steiner, G., Feist, F., and Müller, U. (2018). Measuring Poisson's ratio: mechanical characterization of spruce wood by means of non-contact optical gauging techniques. *Wood Sci. Technol.* 52 (6): 1451–1471.

Liu, T. (1993). Creep of wood under a large span of loads in constant and varying environments. *Holz Roh- Werkst.* 51 (6): 400–405.

Maas, J. M. and Wittel, F. K. (2025). Comprehensive creep compliance characterization of orthotropic materials using an automated system. *Holzforschung* 79 (2-3): 116–133.

Maas, J. M. and Wittel, F. K. (2026). Dataset to "From Elasticity to Creep: Orthotropic moisture-dependent Rheology of Norway Spruce". Zenodo. doi:10.5281/zenodo.18303588.

Mackenzie-Helnwein, P., Eberhardsteiner, J., and Mang, H. A. (2003). A multi-surface plasticity model for clear wood and its application to the finite element analysis of structural details. *Comput. Mech.* 31 (1-2): 204–218.

Maksimov, R. D., Mochalov, V. P., and Urzhumtsev, Yu. S. (1972). Time — Moisture superposition. *Polymer Mech.* 8 (5): 685–689.

McCrum, N. G. and Pogany, G. A. (1970). Time-temperature superposition in the α region of an epoxy resin. *J. Macromol. Sci. B* 4 (1): 109–125.

Milch, J., Tippner, J., Sebera, V., and Brabec, M. (2016). Determination of the elasto-plastic material characteristics of Norway spruce and European beech wood by experimental and numerical analyses. *Holzforschung* 70 (11): 1081–1092.

Müller, U., Ringhofer, A., Brandner, R., and Schickhofer, G. (2015). Homogeneous shear stress field of wood in an Arcan shear test configuration measured by means of electronic speckle pattern interferometry: Description of the test setup. *Wood Sci.Technol.* 49 (6): 1123–1136.

Neuhaus, F.-H. (1981). *Elastizitätszahlen von Fichtenholz in Abhängigkeit von der Holzfeuchtigkeit*. PhD thesis. Inst. für Konstruktiven Ingenieurbau, Ruhr-Universität Bochum.

Newville, M., Otten, R., Nelson, A., Stensitzki, T., Ingargiola, A., Allan, D., Fox, A., Carter, F., and Rawlik, M. (2025). LMFIT: Non-linear least-squares minimization and curve-fitting for python. Zenodo.

Niemz, P., Clauss, S., Michel, F., Hansch, D., and Hansel, A. (2014). Physical and mechanical properties of common ash (Fraxinus excelsior L.). *Wood Res.* 59 (4): 671–682.

Niemz, P. and Sonderegger, W. (2017). *Holzphysik: Physik des Holzes und der Holzwerkstoffe*. Carl Hanser Verlag GmbH & Co. KG, Munich, Germany.

Niemz, P., Teischinger, A., and Sandberg, D., eds. (2023). *Springer Handbook of Wood Science and Technology*, Springer Handbooks. Springer International Publishing, Cham.

Niemz, P., Teischinger, A., and Sandberg, D., eds. (2025). *Wood Material and Processing Data: The Most Relevant Data, Tables, and Figures*. Springer Nature Switzerland, Cham.

Obara, P. (2018). Verification of Orthotropic Model of Wood. *Arch. Civ. Eng.* 64 (3): 31–44.

Osei-Antwi, M., de Castro, J., Vassilopoulos, A. P., and Keller, T. (2013). Shear mechanical characterization of balsa wood as core material of composite sandwich panels. *Constr. Build. Mater.* 41: 231–238.

Ożyhar, T., Hering, S., and Niemz, P. (2013). Moisture-dependent orthotropic tension-compression asymmetry of wood. *Holzforschung* 67 (4): 395–404.

Peng, H., Zhan, T., Jiang, J., Zhang, Y., Cao, J., and Lu, J. (2022). Comparison of the time-moisture and time-temperature equivalences in the creep properties of Chinese fir. *Wood Mater. Sci. Eng.* 17 (6): 911–917.

Ramberg, W. and Osgood, W. R. (1943). Description of stress-strain curves by three parameters. Technical Note 902, National Advisory Committee for Aeronautics, Washington, DC.

Ross, R., ed. (2021). *Wood handbook - Wood as an engineering material*, general technical report fpl-gtr-282 ed. U.S. Department of Agriculture, Forest Service, Forest Products Laboratory, Madison, WI.

Saft, S. and Kaliske, M. (2011). Numerical simulation of the ductile failure of mechanically and moisture loaded wooden structures. *Computers & Structures* 89 (23-24): 2460–2470.

Schmidt, J. and Kaliske, M. (2006). Zur dreidimensionalen Materialmodellierung von Fichtenholz mittels eines Mehrflächen-Plastizitätsmodells. *Holz Roh- Werkst.* 64 (5): 393–402.

Schniewind, A. P. (1968). Recent progress in the study of the rheology of wood. *Wood Sci. Technol.* 2 (3): 188–206.

Simpson, W. T. (1973). Predicting Equilibrium Moisture Content of Wood by Mathematical Models. *Wood Fiber Sci.* 5 (1): 41–49.

Skaar, C. (1988). *Wood-water relations*, Springer series in wood science. Springer, Berlin u.a.

Stojcevski, F., Hilditch, T., and Henderson, L. C. (2018). A modern account of Iosipescu testing. *Compos. - A: Appl. Sci. Manuf.* 107: 545–554.

Sutton, M. A., Yan, J. H., Tiwari, V., Schreier, H. W., and Orteu, J. J. (2008). The effect of out-of-plane motion on 2D and 3D digital image correlation measurements. *Opt. Lasers Eng.* 46 (10): 746–757.

Taniguchi, Y., Ando, K., and Yamamoto, H. (2010). Determination of three-dimensional viscoelastic compliance in wood by tensile creep test. *J. Wood Sci.* 56 (1): 82–84.

The MathWorks Inc. (2022). *MATLAB version: 9.13.0 (R2022b)*. The MathWorks Inc., Natick, Massachusetts, United States.

Trendelenburg, R. (1955). *Das Holz als Rohstoff*, 2nd ed. Carl Hanser Verlag GmbH & Co. KG, Munich.

Virtanen, P., Gommers, R., Oliphant, T. E., Haberland, M., Reddy, T., Cournapeau, D., Burovski, E., Peterson, P., Weckesser, W., Bright, J., et al. (2020). SciPy 1.0: Fundamental Algorithms for Scientific Computing in Python. *Nat. Methods* 17: 261–272.

Wang, J., Jiang, L., Long, K., Liao, Z., Guo, Z., and Wang, X. (2025). In-situ characterization of the compression failure behavior of Chinese fir wood by using micro-CT and digital volume correlation analysis. *Wood Sci. Technol.* 59 (5): 85.

Yoshihara, H. (2009). Prediction of the off-axis stress-strain relation of wood under compression loading. *Eur. J. Wood Prod.* 67: 183–188.

Yu, T., Khaloian, A., and Van De Kuilen, J.-W. (2022). An improved model for the time-dependent material response of wood under mechanical loading and varying humidity conditions. *Eng. Struct.* 259: 114116.

Zhan, T., Jiang, J., Lu, J., Zhang, Y., and Chang, J. (2019). Temperature-humidity-time equivalence and relaxation in dynamic viscoelastic response of Chinese fir wood. *Constr. Build. Mater.* 227: 116637.

Zhang, Y., Hou, J., Chen, H., Cen, J., Jiang, Z., and Yu, Y. (2024). Time-moisture superposition principle in creep behavior of white oak with various earlywood vessel locations. *Maderas: Cienc. Tecnol.* 26: e1324–e1324.